



HAL
open science

Probing the local magnetic structure of the [FeIII(Tp)(CN)3]- Building block via solid-state NMR spectroscopy, polarized neutron diffraction, and first-principle calculations

Siddhartha De, Alexandrine Flambard, Delphine Garnier, Patrick Herson, Frank H Köhler, Abhishake Mondal, Karine Costuas, Béatrice Gillon, Rodrigue Lescouëzec, Boris Le Guennic, et al.

► To cite this version:

Siddhartha De, Alexandrine Flambard, Delphine Garnier, Patrick Herson, Frank H Köhler, et al.. Probing the local magnetic structure of the [FeIII(Tp)(CN)3]- Building block via solid-state NMR spectroscopy, polarized neutron diffraction, and first-principle calculations. Chemistry - A European Journal, 2019, 25 (52), pp.12120-12136. 10.1002/chem.201902239 . hal-02280844

HAL Id: hal-02280844

<https://univ-rennes.hal.science/hal-02280844>

Submitted on 27 Sep 2019

HAL is a multi-disciplinary open access archive for the deposit and dissemination of scientific research documents, whether they are published or not. The documents may come from teaching and research institutions in France or abroad, or from public or private research centers.

L'archive ouverte pluridisciplinaire **HAL**, est destinée au dépôt et à la diffusion de documents scientifiques de niveau recherche, publiés ou non, émanant des établissements d'enseignement et de recherche français ou étrangers, des laboratoires publics ou privés.

Probing the Local Magnetic Structure of the [Fe^{III}(Tp)(CN)₃]⁻ Building Block via Solid-State NMR, Polarized Neutron Diffraction and First Principle Calculations

*Siddhartha De^a, Alexandrine Flambar^d, Delphine Garnier^a, Patrick Herson^a, Frank H. Köhler^b,
A. Mondal^a, Karine Costuas^c, Béatrice Gillon^{d*}, Rodrigue Lescouëzec^{a*}, Boris Le Guennic^{c*},
Frédéric Gendron^{c*}*

^a Sorbonne Université, Institut Parisien de Chimie Moléculaire, CNRS UMR 8232, 4 place
Jussieu, 75252 Paris cedex 5, France

^b Technische Universität München, Lichtenbergstrasse 4, 85747 Garching, Germany

^c Univ Rennes, CNRS, ISCR (Institut des Sciences Chimiques de Rennes) UMR 6226, F-35000
Rennes, France

^d Laboratoire Léon Brillouin, CEA and CNRS, UMR 12, Centre d'Etudes de Saclay, F-91191
Gif-sur-Yvette, France

KEYWORDS. Molecular magnetism, Paramagnetic NMR, Polarized Neutron Diffraction, Spin
Density, DFT, Ab-Initio Calculations

ABSTRACT. We have investigated the local magnetic structure in the $[\text{Fe}^{\text{III}}(\text{Tp})(\text{CN})_3]^-$ building block by combining paramagnetic Nuclear Magnetic Resonance (pNMR) spectroscopy and Polarized Neutron Diffraction (PND) with first principle calculations. The use of the pNMR and PND experimental techniques revealed the spin density extension from the metal to the ligands, and enlightened the different spin mechanisms that take place on the cyanido ligands: spin-polarization on the carbon atoms and spin-delocalization on the nitrogen ones. The results were confronted to theoretical calculations that allowed further analyses. Our combined density functional theory (DFT) and multi-reference calculations are in good agreement with the PND results and the experimental NMR chemical shifts, showing the validity of the theoretical approach. Moreover, the calculations allow us to connect the experimental spin-density map characterized by PND and the suggested repartition of the spin density on the ligands observed by NMR spectroscopy. Interestingly, significant differences are observed between the pseudo-contact contributions of the chemical shifts obtained by theoretical calculations and the values derived from NMR using a simple point-dipole model. **These discrepancies allow underlying the limitation of the point-dipole model, and the need of using more elaborated approaches in order to break down the experimental pNMR chemical shifts into contact and pseudo-contact contributions.**

INTRODUCTION

The design of magnetic materials based on the self-assembly of paramagnetic building blocks has allowed obtaining a great variety of magnetic systems with tunable architecture, topology and dimensionality.¹ The main interest of molecule-based magnetic materials lays in the observation of original magnetic behaviors that are not usually observed in classical magnets. For example, the observation of magnetic bistability in discrete or one-dimensional complexes showing uniaxial magnetic anisotropy (so-called “single-molecule magnets”, SMM or “single-chain magnets”, SCM) has attracted a lot of interests in the last two decades because of the potential use of SMM and SCM as molecular memories.^{2,3,4} The photomagnetism, which is the control of magnetization by light, is another appealing phenomenon that can be observed in molecular materials. In this field, cyanido coordination chemistry has been particularly

successful. One of the reasons is the ability of the cyanido bridging ligand to efficiently promote electronic communication (or electron transfer) between different metal ions. The access to cyanido building blocks with adjustable electronic properties is also an asset in designing molecular magnetic systems.^{5,6} In the early 2000s, some of us synthesized various $[\text{Fe}(\text{L})(\text{CN})_x]^-$ building blocks (L = polydentate ligands, $x = 3-4$) allowing the preparation of low dimensional magnetic systems.⁷ In particular, we reported the preparation of the low-spin Fe(III) building block $[\text{Fe}^{\text{III}}(\text{Tp})(\text{CN})_3]^-$, where Tp^- is the hydrotris(pyrazolyl)borate scorpionate ligand (see Figure 1).⁸ Here the versatility of the scorpionate ligands permits the adjustment of the steric and electronic properties of the precursor, and hence allows tuning the magnetic properties. The use of $[\text{Fe}^{\text{III}}(\text{Tp})(\text{CN})_3]^-$ has been fruitful, in particular for obtaining photomagnetic molecules, SMM and multifunctional systems.^{9,10,11,12,13}

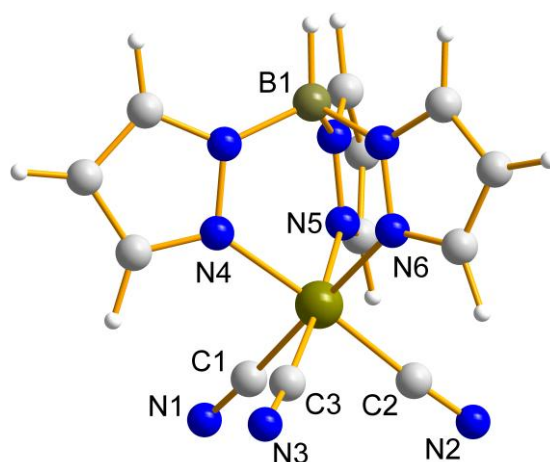


Figure 1. Molecular representation of the building block $[\text{Fe}^{\text{III}}(\text{Tp})(\text{CN})_3]^-$. (Color scheme: green for Fe, blue for N, grey for C, pink for B, white for H.) The magnetization axis c^* used in PND measurements is represented in red. **THE FIGURE STILL NEED TO BE RE-DRAWN !**

A few years ago, we have undertaken a fundamental study, which aims at getting a deeper understanding of the properties of the $[\text{Fe}^{\text{III}}(\text{Tp})(\text{CN})_3]^-$ building block by probing the magnetism at the local scale.¹⁴ Indeed, magnetic properties of molecular materials are mostly obtained from bulk measurements that only give access to macroscopic behavior. The rationalization of these macroscopic magnetic properties is then commonly addressed by phenomenological approaches based on spin Hamiltonian models.¹⁵ For example, EPR spectroscopy can also lead to interesting

local information such as the magnetic anisotropy of the ground state. However, the analysis of the EPR data relies on effective Hamiltonian (g-tensors and /or zero-field splitting parameters).^{16,17} In contrast, in our previous study on the $[\text{Fe}^{\text{III}}(\text{Tp})(\text{CN})_3]^-$ complex, we managed to access to a direct picture of the magnetic anisotropy at the local scale by using a new experimental approach, namely polarized neutron diffraction (PND). We have shown that PND analyses on a single crystal (at moderate fields and in three orthogonal directions) give access to the magnetic susceptibility tensor, and we obtained a direct picture of the magnetic anisotropy on the iron ion, revealing a strong axial anisotropy along the C_3 pseudo-axis.¹⁴

In the present work, we continue exploring techniques that allow probing the magnetic properties at the local scale. More particularly, we focus on techniques that allow probing the spin density distribution in metal complexes. In cyanido building blocks, the spin density delocalization on the cyanido ligand into σ - and/or π -type orbitals is of particular interest as it is related to the magnetic exchange interaction in the resulting self-assembled materials. Only few techniques give access to such local magnetic information. X-ray Magnetic Circular Dichroism (XMCD) is a unique tool to evaluate the respective contributions of the spin and orbit magnetic moment.¹⁸ However, it often fails in providing information for the light atoms, which bear very weak magnetic moments. When suitable crystals are available, PND becomes a powerful alternative to get information on the spin density distribution in paramagnetic complexes. A large panel of complexes with various cyanido building blocks have been already investigated by this technique, but very approximate information was obtained on the spin density extension on the ligands.^{19,20,21} In order to gain information on the ligand spin density distribution, experimental diffraction analysis techniques can be also combined with quantum chemistry.^{22,23} Another experimental alternative method is NMR spectroscopy. This technique is well known as a powerful local structural probe. In the study of paramagnetic systems, it often needs to be combined with ab-initio calculation to link structural environment to paramagnetic chemical shifts. Example can be found with numerous kind of paramagnetic systems including lanthanide-based systems,^{24,25,26} or in solid-state systems²⁷ like Li-ion batteries.^{28,29,30} However, NMR experiments can also be used to probe the spin-density distribution in molecular compounds as a fraction of the NMR chemical shift via the Fermi-contact contribution, which is directly linked to the spin density on the probed atoms. From an experimental point of view, the challenge consists in finding reliable way to evaluate the pseudo-contact (or dipolar) contribution of the

paramagnetic chemical shift, to extract the Fermi-contact term from the paramagnetic chemical shift. Some of us previously used simple models based on the point-dipole approximation to carry out such studies on cyanide-based materials such as hexacyanometallate and Prussian blue analogues,^{31,32,33} but none of these previous works were confronted to ab-initio calculations. Here we propose to investigate the $[\text{Fe}^{\text{III}}(\text{Tp})(\text{CN})_3]^-$ complex and confront experimental NMR results to ab-initio calculations and to PND studies.

To our knowledge, this is the first time that such study combining both NMR and PND techniques to quantum calculation is carried out for probing local magnetic data. The advantage of combining these three techniques was threefold. Firstly, it allowed us drawing a clear picture of the spin density distribution in a strongly paramagnetic system, and secondly, to highlight the different spin mechanisms that govern this distribution. Finally, the combination of these techniques allowed us to reveal the limits of using paramagnetic NMR shifts to access to local spin density (in particular the limits of the point-dipole model in the pseudo-contact/Fermi-contact separation of the paramagnetic NMR shifts) and to propose an approach that can lead to more satisfactory results.

Experimental Details.

Syntheses. All chemicals and solvents (analytical grade) were obtained from chemical providers and used without further purification. The potassium salts of the hydrotris(pyrazolyl)borate and hydrotris(3,5-dimethyl-1-pyrazolyl)borate ligands (Tp and Tp*)³⁴ and the paramagnetic $\text{PPh}_4[\text{Fe}(\text{Tp})(\text{CN})_3]$ complex were obtained as previously described in the literature.³⁵ Large single crystals suitable for the PND experiment were directly obtained by slow evaporation of concentrated solution. Elemental analyses were determined by the microanalytical laboratory of ISCN, Gif-sur-Yvette. FT-IR spectra were collected in the 400-4000 cm^{-1} range with a tensor 27 Bruker FT-IR spectrometer working in the ATR mode.

$\text{PPh}_4[\text{Co}(\text{Tp}^*)(\text{CN})_3] \cdot 3\text{H}_2\text{O}$. A solution of KTp^* (4 mmol) in 80 mL in THF was added dropwise to a solution of $\text{CoCl}_2 \cdot 6\text{H}_2\text{O}$, (4 mmol, 952 mg) under inert atmosphere. After stirring for 1 hour the resulting violet solution, KCN (13.2 mmol, 860 mg) dissolved in a MeOH/H₂O

mixture (1/2) was added to lead to a yellow-orange solution. After stirring overnight, the solution was filtered and left in air. Slow evaporation of the filtrate afforded yellow cubic crystals that were recrystallized from MeCN. Yield 68%. Characteristic stretching vibrations are measured at $\nu_{\max} = 2531 \text{ cm}^{-1}$ (BH stretching) and 2133 cm^{-1} (CN stretching). This last vibration is indicative of the cobalt redox state +III ($\nu_{\text{CN}} > 2115 \text{ cm}^{-1}$ for non-bridging Co^{III} -CN moieties). Other strong and medium peaks are observed at 1547, 1482, 1434, 1416, 1314, 1209, 1106, 1063 cm^{-1} . Elemental analyses for $\text{C}_{42}\text{H}_{48}\text{BPCoN}_9\text{O}_3$: calcd (%) C, 60.95; H, 5.85; N, 15.23. Found: C, 61.22; H, 5.65, N, 15.04. The isotopically enriched cyanido complexes were synthesized at the 1 mmol scale by following the same procedures and by using K^{13}CN and KC^{15}N (each 98% enriched, from Cortecnet, Voisins-le-Bretonneux, France) as starting material.

NMR Spectroscopy Measurements. All the solution and solid-state NMR spectra were measured with Bruker Avance spectrometers. The solid-state NMR spectra were acquired using the magic angle spinning (MAS) technique, by rotating the sample at $\theta \approx 54.74^\circ$ relative to the magnetic field. The acquired spectra showed isotropic chemical shift, δ^{exp} , and a spinning sideband pattern, regularly spaced by the spinning rate, ν_r . The chemical shift anisotropy (CSA) tensor parameters were determined using the module “Solids Line Shape Analysis” from Bruker’s software package Topspin.

In the present work, we used the Haeberlen-Mehring-Spiess convention to describe the principal components of the Chemical Shift anisotropy tensor.^{36,37} The experimental isotropic shifts are $\delta^{\text{exp}} = (\delta_{xx}^{\text{exp}} + \delta_{yy}^{\text{exp}} + \delta_{zz}^{\text{exp}})/3$, where δ_{xx}^{exp} , δ_{yy}^{exp} and δ_{zz}^{exp} are the principal components of the chemical shift tensor [ordered as $|\delta_{zz}^{\text{exp}} - \delta^{\text{exp}}| \geq |\delta_{xx}^{\text{exp}} - \delta^{\text{exp}}| \geq |\delta_{yy}^{\text{exp}} - \delta^{\text{exp}}|$]. Further tensor describing parameters include the anisotropy $\Delta\delta^{\text{exp}} = \delta_{zz}^{\text{exp}} - (\delta_{xx}^{\text{exp}} + \delta_{yy}^{\text{exp}})/2$ and the asymmetry $\eta^{\text{exp}} = (\delta_{yy}^{\text{exp}} - \delta_{xx}^{\text{exp}})/(\delta_{zz}^{\text{exp}} - \delta^{\text{exp}})$.

The exact measurement of the paramagnetic chemical shift requires measuring a diamagnetic reference, with ideally the same structure. As our attempt to prepare the unknown diamagnetic $\text{PPh}_4[\text{Co}^{\text{III}}(\text{Tp})(\text{CN})_3]$ complex was not successful, we synthesized the related $\text{PPh}_4[\text{Co}^{\text{III}}(\text{Tp}^*)(\text{CN})_3]$ complex, where the Tp ligand is methylated. This complex exhibits the same C_3 symmetry as the paramagnetic $\text{PPh}_4[\text{Fe}^{\text{III}}(\text{Tp})(\text{CN})_3]$ complex and its crystal structure is given below. We assume that the ^{13}C and ^{15}N chemical shifts of the two Co^{III} complexes are

similar as the organic ligand has a small influence on the signals: $\delta(^{13}\text{C}) = 135.1$ ppm and $\delta(^{15}\text{N}) = -83$ and -78 ppm in $[\text{Co}^{\text{III}}(\text{CN})_6]^{3-}$ and $\delta(^{13}\text{C}) = 136$ ppm and $\delta(^{15}\text{N}) = -80.2$ ppm in $[\text{Co}^{\text{III}}(\text{Tp}^*)(\text{CN})_3]^-$. Moreover, these differences are small compared to the overall large signal shift measured in this work.

Samples of ^{15}N - and ^{13}C -enriched $\text{PPh}_4[\text{Co}^{\text{III}}(\text{Tp}^*)(\text{CN})_3]$ and of ^{15}N -enriched $\text{PPh}_4[\text{Fe}^{\text{III}}(\text{Tp})(\text{CN})_3]\cdot\text{H}_2\text{O}$ were prepared using about 100 mg of ground crystals packed in a 4 mm diameter ZrO_2 rotor. Their MAS-NMR spectra were recorded at different magnetic fields: 7.1 and 11.7 T for ^{13}C (Larmor frequencies 75.5 and 125.8 MHz respectively) and at 9.4 T for ^{15}N (Larmor frequency of 40.6 MHz). The ^{15}N MAS-NMR spectra of $\text{PPh}_4[\text{Fe}^{\text{III}}(\text{Tp})(\text{CN})_3]\cdot\text{H}_2\text{O}$ were acquired at $\nu_r = 6$ and 10 kHz. The rotor-synchronized Echo-MAS sequence $90^\circ - \tau_2 - 180^\circ$ was used in order to remove baseline distortion. The 90° pulse length was 5.8 μs and the recycling time was 2 s.

An attempt at recording the ^{13}C MAS-NMR spectra of $\text{PPh}_4[\text{Fe}^{\text{III}}(\text{Tp})(\text{CN})_3]\cdot\text{H}_2\text{O}$ at 7.1 T with 4 and 2.5 mm diameter rotors ($\nu_r = 14$ and 34 kHz, respectively) was made, but due to the large chemical shift anisotropy (up to several thousand ppm), higher spinning rates were necessary. The ^{13}C -enriched $\text{PPh}_4[\text{Fe}^{\text{III}}(\text{Tp})(\text{CN})_3]\cdot\text{H}_2\text{O}$ sample was thus prepared packing about 10 mg of dried ground crystals in a 1.3 mm diameter ZrO_2 rotor. The ^{13}C MAS NMR spectra were recorded at different spinning rates of 60 and 65,5 kHz at 16.4 T (Larmor frequency 176.1 MHz). The one-pulse sequence was used with a single pulse excitation of 2.5 μs and a recycling delay of 200 ms. Despite the large spectral width of 1.8 MHz used, several measurements were done by changing the emission frequency in order to localize the extremely shifted ^{13}C paramagnetic signals. The spectral width was then adjusted to limit baseline distortion. The Echo-MAS sequence could not be used because the magnetic relaxation is too fast in that case. The baseline distortions were manually corrected. Data handling included reverse linear prediction after clipping the first data points, exponential multiplication up to the matched filter, and baseline correction.

The ^{15}N and ^{13}C chemical shifts were measured relative to the external references: adamantane ($\delta(^{13}\text{CH}_2) = 29.5$ ppm relative to $\text{TMS}^{38,39}$) and ammonium nitrate ($\delta(^{15}\text{NH}_4^+) = -358.5$ relative to $\text{CH}_3\text{NO}_2^{40}$).

The spectra were recorded at different spinning rates in order to identify the isotropic signals inside the sideband patterns. For each rate, the temperature was controlled inside the rotor by using nickelocene as internal reference. For all samples, microcrystalline powders of the complexes were thus mixed in a glove box with 3-5 % weight of nickelocene whose ^1H NMR signal shift served as internal temperature standard. The isotropic chemical shift of nickelocene protons in function of the temperature is tabulated in the literature:^{41, 42}

$$T = \frac{-79477}{\delta^{\text{exp}} - 12.89} \quad (1)$$

A proton spectrum was acquired before and after each ^{13}C and ^{15}N measurement in order to check the stability of the inner temperature during the measurement.

As the chemical shifts of the paramagnetic species depend on the temperature, the experimental isotropic shifts at the sample temperature T , the isotropic δ^{exp} , were converted to the isotropic paramagnetic shifts, δ^{pNMR} , by subtracting the isotropic shifts of the diamagnetic reference $\text{PPh}_4[\text{Co}(\text{Tp}^*)(\text{CN})_3]$, δ^{dia} . Since the spectra of the paramagnetic compounds were obtained at slightly different temperatures, δ^{pNMR} was converted to the respective value at the standard temperature 298 K following the Curie law.

Computational Details. The 2017's release of the Amsterdam Density Functional (ADF^{43,44,45}) software package was used to perform Kohn-Sham density functional theory (KS-DFT) single-point energy calculations. These calculations utilized the scalar all-electron zeroth-order regular approximation (ZORA⁴⁶) along with the spin-unrestricted formalism. Several functionals were employed: the PBE^{47,48} functional (Perdew-Burke-Ernzerhof) from the generalized gradient approximation, the hybrid functional B3LYP^{49,50} (Becke, 3-parameters Lee-Yang-Parr) with 20% of exact exchange, and the hybrid functional PBE0^{51,52} with 25% of exact exchange. The influence of the atomic basis set on the calculated properties was also investigated by using either (i) the triple- ζ polarized Slater-type orbital (STO) all-electron basis set with two sets of polarization functions for all atoms (TZ2P⁵³), (ii) the NMR optimized STO JCPL⁵⁴ basis set for the ligand atoms in combination with the TZ2P basis set for the iron center, and (iii) the JCPL basis set for the ligand atoms in combination with the quadruply polarized quadruple- ζ (QZ4P) basis set for the iron atom. The use of different basis sets for the metal center and the ligands

should not generate an unbalanced basis set as the valence basis functions in JCPL are derived from TZ2P. The electronic structure of the ground state (GS) was additionally investigated by using the Natural Bond Order⁵⁵ (NBO 6.0) analysis as implemented in the ADF software package. The natural atomic populations as well as the Natural Localized Molecular Orbitals (NLMOs) were obtained from this analysis.

The magnetic properties, namely the EPR g -factors and the hyperfine coupling constants (HyFCCs) for the ^1H , ^{15}N and ^{13}C , were calculated using the ESR⁵⁶ and NMR^{57,58} modules as implemented in ADF. The EPR g -factors were calculated using a quasi-restricted approach developed by van Lenthe, Wormer and van der Avoird (LWA).⁵⁶ In this case, the spin-orbit coupling is treated variationally within the two-component spin-orbit ZORA formalism. Despite the lack of spin-polarization, this approach has shown to be efficient to properly reproduce the g -factors of Kramers doublet complexes. Introduction of the spin-polarization in the g -factors calculations has been tested in a previous work¹⁴ and did not converged to the correct ground state (see Table S13). The HyFCCs were calculated using a linear response (LR) approach.⁵⁹ In that scenario, a spin-unrestricted scalar relativistic (SR) ZORA calculation is first realized to obtain the SR electronic structure and then, the spin-orbit coupling is added a posteriori by a perturbative treatment. If necessary, the following nuclear g -factors were employed to convert the HyFCCs from atomic units to MHz: $g_{1\text{H}} = 5.5857$, $g_{13\text{C}} = 1.4048$ and $g_{15\text{N}} = -0.2831$. Finally, the NMR chemical shieldings of tetramethylsilane and nitromethane compounds used as references in the paramagnetic NMR calculations were obtained with the NMR module of ADF.⁶⁰

The wavefunction calculations were performed using the Molcas 8.2 software package.⁶¹ In these calculations, the complete active space self-consistent field⁶² (CASSCF) approach and the complete active space perturbation theory at the second order⁶³ (CASPT2) were used to treat the static and dynamic correlation effects, respectively. The CASPT2 calculations were performed using the multi-state approach with an imaginary shift of 0.2 in order to avoid intruder states in the wavefunction. The second-order Douglas-Kroll-Hess^{64,65,66,67} scalar relativistic Hamiltonian was used to treat the scalar relativistic effects in combination with the all-electron atomic natural orbital relativistically contracted (ANO-RCC) basis set from the Molcas library.^{68,69,70} The basis

sets were contracted to the triple- ζ plus polarization (TZP) quality (Fe = 21s15p10d6f4g2h/6s5p3d2f1g; B, N, C = 14s9p5d3f2g/4s3p2d1f; H = 8s4p3d1f/2s1p).

The choice of the active space, namely CAS(9,12), was driven by the previous ab-initio study performed on the compound of interest,⁷¹ and on the results of previous ab-initio studies performed on related complexes with various transition metals.^{72,73,74} This active space corresponds to the five electrons of the Fe³⁺ ion distributed into the five 3d orbitals, augmented by five unoccupied 3d' orbitals in order to properly take into account the double-shell effect. Additionally, two doubly occupied ligand-based orbitals, spanning formally the e_g irreducible representation (irrep) in the O_h symmetry point group, were added. It was shown that these ligand orbitals interact with the metal-centered 3d orbitals of corresponding symmetry in order to form combinations of bonding and antibonding molecular orbitals of σ character.

The calculations employed the state-averaged formalism at the SR level by taking into account one sextet, six quartet and 10 doublet spin states. The spin-orbit coupling (SOC) was then introduced within a state interaction among the basis of calculated SR states using the restricted active space state interaction (RASSI) approach.⁷⁵ Herein the SOC matrix is diagonalized using either the calculated SR CASSCF or SR CASPT2 energies. Therefore, in the manuscript the scalar and spin-orbit coupling results will be denoted as SCF/PT2-SR and SCF/PT2-SO, respectively.

The EPR g -factors were calculated according to Reference 76 as implemented in the RASSI module of Molcas, whereas the magnetic susceptibility calculations were performed using the Single-Aniso module of Molcas as detailed in Reference 77. Finally, the magnetic properties of [Fe^{III}(Tp)(CN)₃]⁻ were analyzed using natural orbitals (NOs), natural spin orbitals (NSOs) and spin magnetizations ($m_u^S(r)$) that were directly obtained from the multi-configurational wavefunctions that include SOC effects. The procedure to obtain these orbitals and densities is explained in the References 78, 79 and 80. The orbitals were then visualized with the graphical interface of the ADF software package.

Spin Density from NMR Spectroscopy Measurements. In paramagnetic species, the experimental chemical shift is the sum of two main contributions:^{81,82}

$$\delta^{\text{exp}} = \delta^{\text{dia}} + \delta^{\text{pNMR}} \quad (2)$$

δ^{dia} is the diamagnetic contribution to the chemical shift (usually independent of T) in the absence of any influence from paramagnetism,⁸³ here obtained from $\text{PPh}_4[\text{Co}^{\text{III}}(\text{Tp}^*)(\text{CN})_3]$ (see Supplementary Information). δ^{pNMR} is the paramagnetic contribution to the experimental chemical shift and is solely due to the presence of unpaired electron(s). More specifically, the δ^{pNMR} term is the sum of a Fermi-contact term (δ^{FC}) and a pseudo-contact (or dipolar) term, δ^{PC} . The pseudo-contact chemical shift is due to a dipolar through-space interaction between the spin and electronic magnetic moments, and as a first approximation, it can be obtained from the following equation:^{83,84,85}

$$\delta^{\text{PC}} = \frac{1}{12\pi r^3} \left[\Delta\chi_{\text{ax}}(3 \cos^2 \theta - 1) + \frac{3}{2} \Delta\chi_{\text{rh}} \sin^2 \theta \cos 2\phi \right] \quad (3)$$

where r is the vector connecting the paramagnetic metal center and the probed nucleus, $\Delta\chi_{\text{ax}}$ and $\Delta\chi_{\text{rh}}$ represent the magnetic susceptibility anisotropy, and θ and ϕ are the polar angles defining the position of the probed nucleus with respect to the frame of the magnetic susceptibility tensor. Alternatively, the magnetic susceptibility can be expressed by using the spin-only formula. In that case the anisotropy is reflected in the main value of the g -tensor. For example, for $S = 1/2$ (low spin Fe(III) ion) with an axial symmetry, the isotropic δ^{PC} can be expressed as:

$$\delta^{\text{PC}} = \frac{\mu_0 \beta_e^2 S(S+1)}{4\pi 9k_B T} \sum_j \frac{3 \cos^2 \theta_j - 1}{r_j^3} (g_{\parallel}^2 - g_{\perp}^2) \quad (4)$$

In this formula, k_B is the Boltzmann constant, T , the temperature, g_{\parallel} and g_{\perp} are the main values of the g tensor, S is the electron spin quantum number, μ_0 is the vacuum permeability, β_e , the Bohr magneton, and all are given in SI units. The value obtained from Equation (3) and (4) can be converted to ppm by a factor of 10^6 . It is important to remember that the validity of these equations only holds if the spin density is localized at the metal center, i. e. no delocalization to other nuclei yielding contact shifts occurs. For instance, Benda *et al.* have shown that the point-dipole approximation could be safely used in the CoMMP-12 protein for atoms located beyond 8 Å of the paramagnetic center.⁸⁶ For closer atoms, the point-dipole approximation breaks down and the estimation of the pseudo-contact term requires quantum calculations of the spin-dipole hyperfine coupling constant.

On the other hand, δ^{FC} is the through-bond interaction called the Fermi-contact term. It is due to the interaction between the spin-density delocalized onto the probed atom and the nuclear

magnetic moment. In other words, it is correlated with the probability of finding the unpaired electron onto the nuclei, and it thus arises from the presence of spin density in the (mostly) valence s orbital of the nucleus.^{83,84} The isotropic Fermi-Contact hyperfine coupling constant, A_s^{FC} , due to the through-bond interaction with the probed nucleus is linked to the isotropic contact shift, δ^{FC} by the equation (assuming an axial anisotropy):

$$\delta^{\text{FC}} = \frac{g_e \beta_e S(S+1)}{3\gamma_X k_B T} A_s^{\text{FC}} F(g_{ii}, D) = \frac{\mu_0}{a_0^3} \frac{\beta_e^2 g_{av}^2 S(S+1)}{9k_B T} \rho_{is}(r) \quad (5)$$

where γ_X is the gyromagnetic constant of the probed nucleus, $F(g_{ii}, D)$ is a function of the components g_{ii} , of the g tensor and the zero-field splitting D . In the case of $S = 1/2$, one gets $F(g_{ii}, D) = 1$. This formula is valid when only one spin state is populated, and when the ground state can be described by a spin quantum number, S . From there, the δ^{FC} can be easily connected to spin-density located in the s orbitals ($\rho_{is}(r)$).^{27,32} It is worth underlying that, according to Equation 5, the sign of the NMR Fermi-contact term provides a straightforward access to the sign of the spin density at the probed nuclei. This allows probing the spin extension mechanisms from the metal ion to the ligands in paramagnetic species.⁸³ Typically, two mechanisms can be considered.²⁸ For the delocalization mechanism, the unpaired electron lies in a hybrid metal-ligand orbital and the spin density sign is conserved over all the atoms involved in the molecular orbital. For the spin polarization mechanism, the spin density sign alternates from one neighboring atom to the other and decreases exponentially.

Ab-Initio Paramagnetic NMR Calculations. The calculated ^1H and ^{13}C isotropic chemical shifts in this work are given with respect to tetramethylsilane (TMS), whereas the ^{15}N isotropic chemical shifts are given with respect to nitromethane. The NMR shielding constants for the references were obtained at the Kohn-Sham density functional theory (KS-DFT) level using the same functional and basis set as used for the probe. The results of these calculations are given in Table S11 of the Supporting Information. Therefore, the calculated isotropic chemical shift (δ_i^{calc}) in units of ppm for a given nuclei (i) with respect to the reference is obtained as:

$$\delta_i^{\text{calc}} = \sigma_i^{\text{ref}} - \sigma_i^{\text{pNMR}} \quad (6)$$

where the NMR shielding constant of the probe (σ_i) can be defined as a sum of two contributions σ_i^{orb} and σ_i^{pNMR} , with the former corresponding to the ‘orbital shielding’ and being independent of the paramagnetism of the complex, and the latter corresponding to the paramagnetic chemical shielding constant. Depending on the nature of the compound of interest, the theory to properly calculate the paramagnetic NMR (pNMR) shielding tensor may take different forms. For more details, the reader is oriented to References 28, 87, 88, 89 and 90. In the case of a complex with a Kramers doublet GS, or a GS with a pseudo-spin $\tilde{S} = 1/2$, which is well separated in energy from the excited states (ESs), i.e. the ESs are not thermally populated, the pNMR shielding tensor can be calculated as:⁸⁷

$$\sigma_i^{\text{pNMR}} = -\frac{\beta_e}{g_N \beta_N} \frac{S(S+1)}{3k_B T} \mathfrak{g} \cdot \mathbb{A} \quad (7)$$

with β_e , g_N , β_N and k_B associated to the Bohr magneton, the nuclear g -factor, the nuclear magneton and the Boltzmann constant, respectively. In Equation (7), \mathfrak{g} corresponds to the Zeeman coupling matrix and is calculated either using wavefunction theory or using KS-DFT, whereas \mathbb{A} is the hyperfine coupling matrix and is obtained from KS-DFT calculations (see the computational details). Such computational strategy has been already applied successfully on a large panel of transition metal complexes.^{91,92,93,94,95,96,97,98,99,100,101} In order to assemble the Zeeman g -tensors, the hyperfine coupling matrices and the orbital shielding, we have used the pNMRShift program developed by the Autschbach group.^{95,96} In addition to obtain the pNMR shielding tensor, the pNMRShift program allows its decomposition into the Fermi-contact (FC) and pseudo-contact (PC) contributions. The reader is reminded that in a non-relativistic framework the FC contribution is related to the amount of spin-density located at the nucleus of interest and is proportional to the scalar product $g_{\text{iso}}A_{\text{iso}}$ in Equation (7). On the other hand, the PC contribution corresponds to a dipolar coupling between the magnetic moments of the metal center and the nuclei (“spin-dipole” mechanism) that is proportional to the anisotropic part of the Zeeman and hyperfine interactions. In the case of a paramagnetic complex that exhibits no spin density delocalization on the ligand atoms, one can assume that the FC contribution tends to zero and only the PC term contributes to the pNMR shift. In that specific scenario, the origin of the paramagnetic NMR shift is purely dipolar and the PC term can be calculated considering a point-dipole approximation (as explained above). However, the extraction of the FC and PC

contributions from the pNMR chemical shifts is usually not straightforward as metal-spin density often leaks on the surrounding ligands. Additionally, relativistic effects, such as spin-orbit coupling (SOC), render more complex this separation of the chemical shifts by introducing anisotropic contributions into the FC term and isotropic contribution into the PC term via contribution into the calculated g-factors and hyperfine coupling constants.⁹⁰

RESULTS

Solid-State ^{13}C and ^{15}N NMR Spectroscopy of $\text{PPh}_4[\text{Fe}^{\text{III}}(\text{Tp})(\text{CN})_3]\cdot\text{H}_2\text{O}$

As the ^{13}C and ^{15}N spectra obtained with $\text{PPh}_4[\text{Fe}^{\text{III}}(\text{Tp})(\text{CN})_3]\cdot\text{H}_2\text{O}$ sample at natural abundance did not yield to satisfactory signal-to-noise ratio and resolution, the compound was prepared by using KC^{15}N and K^{13}CN starting materials (see Supporting Information). We will focus in this section to solid-state spectra as the resolution obtained by MAS technique is much improved in comparison to that observed in solution. For comparison reason, a ^{13}C NMR solution measurement is given in Figure S8.

The ^{13}C MAS NMR spectra were acquired at 60 and 65.5 kHz and are shown in Figures 2 and S6. Superposition of the spectra allowed the determination of the isotropic shift ($\delta_{327.9}^{\text{exp}} = -3726$ ppm).

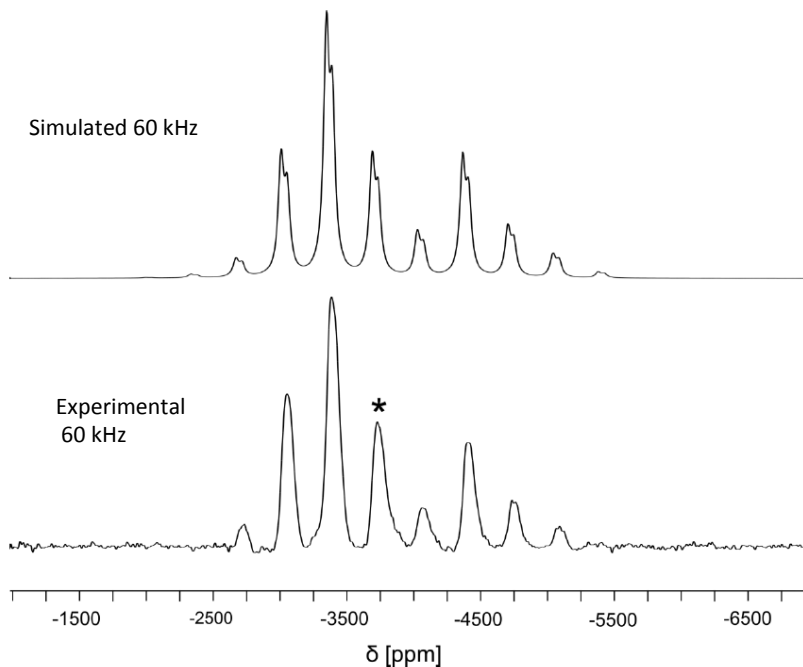


Figure 2. Simulated (top) and experimental (bottom) ^{13}C NMR spectra (16.4 T) of $\text{PPh}_4[\text{Fe}^{\text{III}}(\text{Tp})(\text{CN})_3]\cdot\text{H}_2\text{O}$ acquired at $\nu_r = 60$ kHz and $T = 327.9$ K.

The broad sideband features do not allow distinguishing non-equivalent cyanido ligands likely because the coupling with the ^{14}N quadrupolar nuclei and the dipolar interaction with paramagnetic neighbor ions lead to a significant line broadening, as observed previously for other reported cyanido complexes.^{102,103} The line broadening may also arise from anisotropic bulk magnetic susceptibility and the existence of small gradient temperature in the rotor. However, a significantly better agreement between experimental and simulated spectra was obtained when assuming two different ^{13}CN ligand in the ratio 2/1 (Figure 3). Note that the crystal structure and the ^{15}N NMR studies (see below) show two similar cyanido ligand and a third different one.⁸

As already observed for hexacyanidometallates,^{4,5,103,104,105} the isotropic chemical shifts of the cyanido carbons are strongly shifted to lower frequency compared to their diamagnetic reference. The experimental isotropic shifts deduced from the simulated spectra exhibit high negative values, -3726 and -3755 ppm at 327.9 K, which unambiguously account for negative values of spin density on the carbon cyanido. These values, which are somewhat higher than those measured in $\text{Cs}_2\text{K}[\text{Fe}^{\text{III}}(\text{CN})_6]$, prove that the $\text{Fe}\rightarrow\text{C}$ spin polarization is more important than the direct delocalization mechanism, as it has been observed in previous studies of

hexacyanometallates.^{102, 106} This result is also fully consistent with the PND results and theoretical calculations (see below), which both indicate a negative spin density on the carbon atoms.

The parameters of the ^{13}C chemical shift tensors are reported in Table 1. The presence of spin density does not affect the tensor symmetry, which remains strongly axial, as for the diamagnetic $\text{PPh}_4[\text{Co}^{\text{III}}(\text{Tp}^*)(\text{CN})_3]$ model complex. In contrast the extension of the chemical shift anisotropy (CSA) determined at $\nu_r = 60$ kHz is about 3000 ppm, which is tenfold larger than that of the diamagnetic $\text{PPh}_4[\text{Co}^{\text{III}}(\text{Tp}^*)(\text{CN})_3]$ reference. The extension is also larger than that measured in the octahedral $\text{Cs}_2\text{K}[\text{Fe}^{\text{III}}(\text{CN})_6]$ (*ca.* 1400 ppm), which reflects a greater dissymmetry around the ^{13}C atoms.

As expected because of the higher distances from the paramagnetic source, the ^{15}N NMR spectra exhibit a better spectral resolution. **It has to be mentioned that the lower gyromagnetic ratio of ^{15}N is also improving the spectral resolution.** The superposition of the 6 and 10 kHz spectra allows the determination of three clearly defined isotropic ^{15}N signal at $\delta^{\text{exp}} = 522, 502$ and 474 ppm (Figures 3 and S7). These peaks can be ascribed to three different cyanido groups (determined by X-Ray diffraction analysis⁸) of the Fe(III) complex, although no specific attribution can be done. The positive paramagnetic contribution corresponds to a positive spin density perceived by the nitrogen nuclei. The result is consistent with previous paramagnetic NMR studies on hexacyanometallates and it is expected when both direct delocalization and spin polarization place positive spin density at the N atom.^{4,107,108}

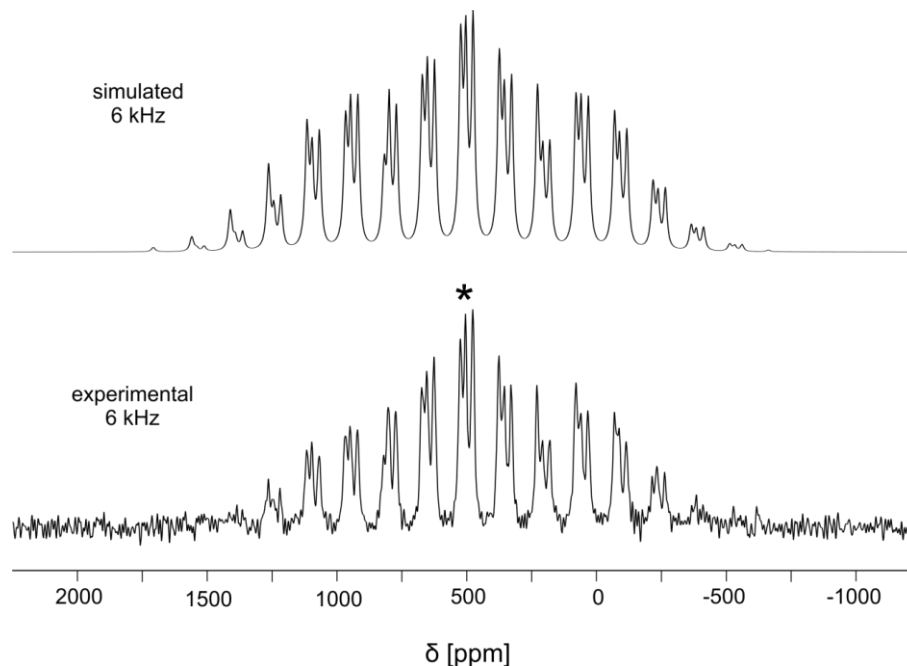


Figure 3. Simulated (top) and experimental (bottom) ^{15}N MAS-NMR spectrum (9.4 T) of $\text{PPh}_4[\text{Fe}^{\text{III}}(\text{Tp})(\text{CN})_3]\cdot\text{H}_2\text{O}$, $\delta(\text{NiCp}_2) = -245.9$ ppm ($T = 307.1$ K) and $\nu_r = 6$ kHz.

The 6 kHz simulated spectrum is shown in Figure 3. Interestingly, ^{15}N spectra of this compound do not exhibit the same symmetry as that of the diamagnetic reference. Indeed, while the Co(III) complex exhibits strongly axial **chemical shift anisotropy (CSA, see experimental section)** tensors (mean asymmetry parameter $\eta = 0.087$), the Fe(III) species clearly exhibits non-axial contributions, with η ranging from 0.785 to 0.912.

The extension of the **CSA** amounts to *ca.* 2000 ppm, which is slightly higher than that measured in the $\text{K}_3[\text{Fe}(\text{CN})_6]$ (*ca.* 1900 ppm) and $\text{Cs}_2\text{K}[\text{Fe}^{\text{III}}(\text{CN})_6]$ (*ca.* 1600 ppm), indicating as for the ^{13}C atoms a greater anisotropy around the ^{15}N atoms.

It is worth noticing that the CSA tensors of the ^{15}N cyanido atoms in $[\text{Fe}^{\text{III}}(\text{Tp})(\text{CN})_3]^-$ have a low symmetry (see Table 1). If the shift anisotropies are visualized by spheroids, they would be clearly prolate at C atoms and scalene (with three different axes) at N atoms. This contrasts with the axial symmetry of the ^{15}N CSA tensor observed in both the diamagnetic $[\text{Co}^{\text{III}}(\text{Tp}^*)(\text{CN})_3]^-$ reference, and in the paramagnetic $[\text{Fe}^{\text{III}}(\text{CN})_6]^{3-}$ parent complex. The lower symmetry observed in the ^{15}N CSA tensor is to be correlated to the lower symmetry of the $\text{PPh}_4[\text{Fe}^{\text{III}}(\text{Tp})(\text{CN})_3]\cdot\text{H}_2\text{O}$

as compare to the $[\text{Fe}^{\text{III}}(\text{CN})_6]^{3-}$ complex and to the strong magnetic anisotropy of that complex as shown in our previous PND study.¹⁴

Table 1. Measured isotropic Chemical shifts (δ^{exp} , in ppm) and its tensor parameters (δ_{uu}^{exp} , in ppm) of $\text{PPh}_4[\text{Fe}^{\text{III}}(\text{Tp})(\text{CN})_3]\cdot\text{H}_2\text{O}$. The isotropic pNMR chemical shifts converted at 298K (δ^{pNMR} , in ppm) are also given for comparison.

$[\text{Fe}^{\text{III}}(\text{Tp})(\text{CN})_3]^-$	^{13}C			^{15}N	
δ^{exp}	-3726	-3755	522	502	474
δ_{zz}^{exp}	-5159	-5110	-356	-345	-380
δ_{yy}^{exp}	-3016	-3081	401	579	512
δ_{xx}^{exp}	-3003	-3074	1518	1273	1292
η^{exp}	0.009	0.005	0.785	0.819	0.912
δ^{pNMR}	-4249	-4281	621	600	571

Experimental chemical shifts are given at 327.9 K (^{13}C) and 307.1 K (^{15}N) while the paramagnetic one is converted to 298 K (see Equation 1).

Solution ^1H NMR Spectroscopy of $\text{PPh}_4[\text{Fe}^{\text{III}}(\text{Tp})(\text{CN})_3]\cdot\text{H}_2\text{O}$

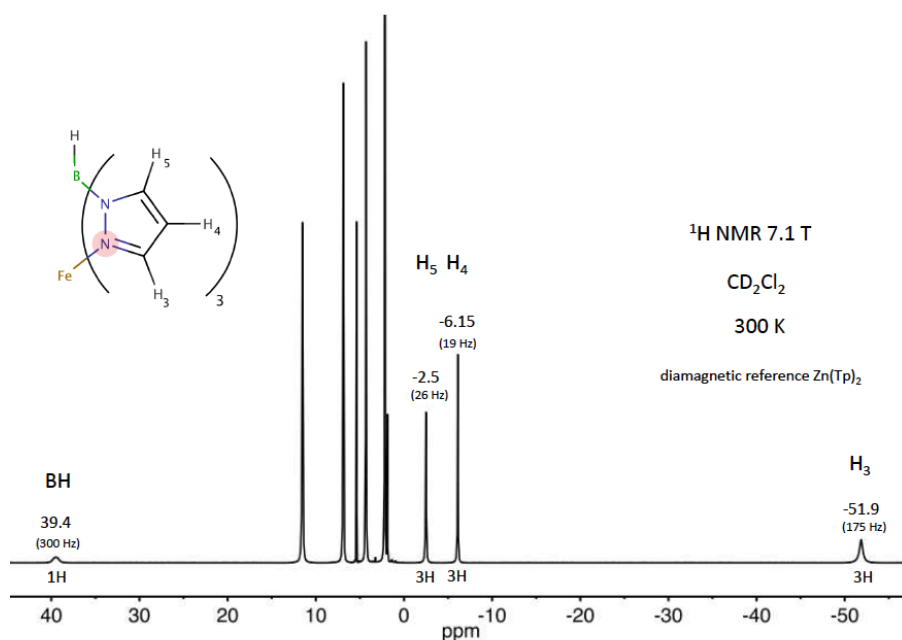


Figure 4. ^1H NMR spectrum (9.4 T) of $\text{PPh}_4[\text{Fe}^{\text{III}}(\text{Tp})(\text{CN})_3]\cdot\text{H}_2\text{O}$ at 300 K (signals in the diamagnetic region are due to the PPh_4 counter ions, the solvent peak, and residual solvents).

While the ^{13}C solution NMR spectrum of the enriched $\text{PPh}_4[\text{Fe}^{\text{III}}(\text{Tp})(\text{CN})_3]\cdot\text{H}_2\text{O}$ leads to broad features in comparison to solid-state spectra (Figure S8), the opposite situation occurs with the proton NMR (Figure S9) because of the proton-proton dipolar coupling. In contrast, in solution molecular tumbling yields well resolved isotropic signals (Figure 4). The proton signal assignment reported in Figure 4 is based on the intensity of the signal and their half widths. The protons that are close to the paramagnetic source are expected to be broader because of the dipolar contribution to the relaxation. The paramagnetic chemical shifts were obtained by taking as a reference the diamagnetic complex $[\text{Zn}(\text{Tp})_2]$.

Spin Density from NMR Measurements.

In order to extract the spin density values, the pseudo-contact contribution (δ^{PC}) to the paramagnetic chemical shift was first calculated using Equation (4). The distances between the paramagnetic metal ion and the probed nuclei (r_j) were directly extracted from the crystal structure data.⁸ As the ^{13}C and ^{15}N signal cannot be assigned to specific cyanido ligand, we used the extrema values of r_j to estimate the dipolar contribution range: r_j values range from *ca.* 1.91 Å to 1.93 Å for $\text{Fe}^{\text{III}}\text{-C}$ and from 3.04 Å to 3.07 Å for $\text{Fe}^{\text{III}}\text{-N}$. For the proton signals, as a complete assignment of the ^1H spectrum was obtained, specific r_j values were extracted for each proton and used for the calculation. The g_i values, which are also required to estimate the pseudo-contact contribution, were already reported in a previous EPR measurement:¹⁴ $g_x = 1.1$, $g_y = 0.57$ and $g_z = 3.7$. It is worth mentioning that the g tensor values were obtained at 5 K and thus reflect the magnetic anisotropy at low temperature. In contrast, NMR experiments are performed near room temperature, where anisotropy should be weaker (for example the g tensor anisotropy is much smaller at 100 K than at 20 K in $\text{K}_3[\text{Fe}(\text{CN})_6]$).¹⁰⁹ In order to have a better approximation of the magnetic anisotropy at 298 K, we thus estimated the pseudo-contact contribution by using the calculated magnetic susceptibility, which led to $g_x = 2.05$, $g_y = 1.98$ and $g_z = 4.17$ at 300 K (see Supporting Information). A comparison of calculations using either low-temperature EPR data or the simulated g_{ii} value at 298 K is given in Table 2.

Here we benefit from our previous PND study on single crystals of $\text{PPh}_4[\text{Fe}(\text{Tp})(\text{CN})_3]\cdot\text{H}_2\text{O}$, which proves that the magnetic anisotropy is strongly axial with an easy axis very close to the

Fe-B axis.¹⁴ Thus the angles θ_j (the angle between magnetic axis and r_j) are also known in the present study. The θ_j angles range from 124.5° to 127.3° for ¹³C and from 122.6° to 127.1° for ¹⁵N. There is a significant influence of θ_j and r_j on the Fe-¹³C and Fe-¹⁵N dipolar contribution of PPh₄[Fe^{III}(Tp)(CN)₃].H₂O. In principle, an unpaired electron located on the Fe(III) ion can induce a dipolar contribution up to *ca.* +640 ppm ($\theta_j = 90^\circ$) or -320 ppm ($\theta_j = 0^\circ$) at the cyanido carbons, *ca.* 1.92 Å away. Since nitrogen lies farther from the Fe(III) ion, the pseudo-contact contributions to the paramagnetic chemical shift is smaller, but it can still range from +158 ppm to -79 ppm (using low temperature EPR data). However, in the case of the [Fe^{III}(Tp)(CN)₃]⁻ complex, the geometry is fortuitously favorable with θ_j angles close to 124° resulting in weak value of $(3\cos^2\theta-1)$, and weak value of the pseudo-contact chemical shifts. Using the experimental data mentioned above, the pseudo-contact contributions (within the point dipole approximation) of the ¹³C cyanido atom are in the range *ca.* -11.6 to +32.8 ppm, while those of the ¹⁵N cyanido atom range from -9.9 to +7.3 ppm. The use of the simulated g_{ii} values, derived from the **calculated magnetic susceptibility at 298K**, slightly affects these ranges (see Table 2). Overall these values remain moderate in comparison to the experimental chemical shifts and have no impact on the spin density estimates (see Table 2 and details below). In contrast, the pseudo-contact contributions of the protons (calculated using the exact location of the nuclei with respect to the magnetic axis and the metal ion) are very dependent from one proton to the other, and can be very important in comparison to the experimental chemical shift (Table 2). The use of either the low-temperature EPR data or the simulated g_{ii} values at **298 K** leads to significantly different values of the dipolar contribution.

For all the nuclei, the contact term is further deduced by subtracting the pseudo-contact contribution from the paramagnetic chemical shift (see Equation 2). Since chemical shifts of paramagnetic species are strongly dependent upon temperature and since the spectra were acquired at a different temperature, direct comparison of raw data cannot be performed. The chemical shifts have to be rescaled to match to a common temperature for all the data. As the Curie law is valid near room temperature for the [Fe^{III}(Tp)(CN)₃]⁻ complex, one can calculate the corresponding isotropic Fermi-contact contribution to the chemical shift at 298 K:^{108,110}

$$\delta^{FC} = [(\delta^{exp} - \delta^{dia}) T/298] - \delta^{PC} \quad (8)$$

Here δ^{dia} is 136 ppm for the ^{13}C and -80.3 ppm for the ^{15}N . As the ^{13}C and ^{15}N NMR signal cannot be specifically assigned to a given atom, the spin density calculation were carried out by taking into account two extreme values of the experimental chemical shift. The two extreme values of the pseudo-contact contribution were then subtracted to the paramagnetic chemical shift values to obtain the largest spin density range. The spin density (in a.u.⁻³) and the unpaired electron fraction are reported in Table 2. Here, for the ^{13}C and ^{15}N nuclei, we assumed that the spin is in the valence $2s$ orbital. The involvement of $1s$ orbitals through cross terms with $2s$ orbitals is not excluded, but that should not affect the general conclusions.

Table 2. Isotropic Pseudo-Contact (δ^{PC}), Fermi-Contact (δ^{FC}) chemical shifts, s orbital spin density value (ρ_s) of the ^{13}C and ^{15}N atoms ($2s$ orbital), ^1H atoms ($1s$ orbital) and fraction of electron in s orbital (f_s) of compound $\text{PPh}_4[\text{Fe}(\text{Tp})(\text{CN})_3]\cdot\text{H}_2\text{O}$.^(a)

	^{13}C	^{15}N	H_3	H_4	H_5	BH
$\delta^{PC(b)}$	-11.6 / +36.5	-9.9 / +7.3	-60.70	-4.60	13.90	64.80
$\delta^{PC(c)}$	-8.6 / + 27.0	-7.4 / +5.4	-44.90	-3.40	10.30	47.80
$\delta^{FC(b)}$	-4317 / -4237	563 / 630	1.27	-7.73	-24.20	-35.20
$\delta^{FC(c)}$	-4308 / -4240	570 / 620	-14.60	-8.93	-20.60	-18.20
$\rho_s^{(b)}$	-0.0197 / -0.0200	0.0026 / 0.0029	$5.7 \cdot 10^{-6}$	$-36.2 \cdot 10^{-6}$	$-112 \cdot 10^{-6}$	$-162 \cdot 10^{-6}$
$\rho_s^{(c)}$	-0.0197 / -0.0200	0.0026 / 0.0029	$-72.0 \cdot 10^{-6}$	$-41.7 \cdot 10^{-6}$	$-94.4 \cdot 10^{-6}$	$-80.0 \cdot 10^{-6}$
$f_s^{(b)}$	-0.0044 / -0.0045	0.00033 / 0.00037	$+1.3 \cdot 10^{-6}$	$-8.03 \cdot 10^{-6}$	$-25.1 \cdot 10^{-6}$	$-35.2 \cdot 10^{-6}$
$f_s^{(c)}$	-0.0044 / -0.0044	0.00033 / 0.00037	$-15.2 \cdot 10^{-6}$	$-9.28 \cdot 10^{-6}$	$-21.4 \cdot 10^{-6}$	$-20.4 \cdot 10^{-6}$

(a) Chemical shifts are given in ppm for $T = 298\text{K}$, and spin density values in (a.u.)⁻³; (b) estimates obtained by using g_{ii} values from EPR at 5K; (c) estimates obtained by using the simulated g_{ii} value at 298 K and Equation S9.

As the pseudo-contact contribution is very weak for both ^{13}C and ^{15}N cyanido atoms, the use of low-temperature EPR data or simulated g_{ii} values has no actual impact on the results. It is observed by NMR that the $[\text{Fe}^{\text{III}}(\text{Tp})(\text{CN})_3]^-$ complex exhibits negative spin density in the cyanido carbon $2s$ orbitals, and a positive one at the cyanido nitrogen atoms. This observation is in agreement with the PND study on $\text{PPh}_4[\text{Fe}^{\text{III}}(\text{Tp})(\text{CN})_3]\cdot\text{H}_2\text{O}$ and the theoretical calculations (*vide infra*). This points to a dominant spin-polarization mechanism from the paramagnetic ion to the cyanido carbon atoms (negative spin density) and on the contrary a spin-delocalization mechanism to the cyanido nitrogen atoms (positive spin density) as observed in the hexacyanometallates.^{31,102} On one hand, the polarization mechanism of the M-C link (z axis) is consistent with the retained axial symmetry of the ^{13}C MAS-NMR spectra. On the other hand,

the low symmetry (rhombic) of the ^{15}N CSA tensors in the $[\text{Fe}^{\text{III}}(\text{Tp})(\text{CN})_3]^-$ complex suggests that the two orthogonal $t_{2g}\text{-p}_x$ $t_{2g}\text{-p}_y$ delocalization pathways are not equivalent (in contrast with the $[\text{Fe}^{\text{III}}(\text{CN})_6]^{3-}$ complex). The axial symmetry of the ^{15}N tensor observed in the diamagnetic model also confirms that the lower symmetry of the tensor arises from the presence of the paramagnetic contribution to the CSA.

The mean electron spin density located on the 2s orbital of cyanido carbon atoms of $[\text{Fe}^{\text{III}}(\text{Tp})(\text{CN})_3]^-$, ca. -0.020 a.u.^{-3} is close to that previously measured on the $[\text{Fe}^{\text{III}}(\text{CN})_6]^{3-}$ (ca. -0.025 a.u.^{-3}), suggesting that the polarization of the Fe-C bond is not significantly affected by the replacement of the cyanido groups by the Tp ligand. These values are also in good agreement with those obtained from PND and DFT analysis (see below).

In absolute values, the electron spin density located in the 2s orbitals of the cyanido nitrogen atoms, ca. 0.0028 a.u.^{-3} , is smaller than that found by ^{15}N MAS-NMR in the 2s orbitals of the nitrogen atoms of the hexacyanometallates (ca. $+0.0064 \text{ a.u.}^{-3}$). This suggests a less favorable orbital overlap between the π^* orbitals of the cyanido fragments and the iron orbitals of the $[\text{Fe}^{\text{III}}(\text{Tp})(\text{CN})_3]^-$. The spin density values are also qualitatively coherent with the present PND results and theoretical calculations (see below).

The spin density on the C and N atoms of the Tp ligand could not be extracted as no ^{13}C or ^{15}N NMR signals were detected because of their low abundances (non enriched Tp ligand). However, spin densities values measured on the proton nuclei have been estimated. These values are much weaker than those measured on the cyanido ligand. This is as expected, because the protons are localized at remote position on the organic ligand and because the spin density is transmitted from the C pyrazolyl atoms to the protons through a polarization mechanism. One could also expect weaker spin density on the Tp ligand in comparison to the cyanido ones, because of the weaker covalency of the Fe-N(Tp) bonds (CN is a strong σ -donor π -acceptor ligand while Tp is a σ donor ligand). Finally, it is worth underlying that the calculated spin density values obtained by NMR on the protons depend on the calculation of the dipolar contribution. As shown in Table 2, the spin density values obtained by using the g_{\parallel} and g_{\perp} obtained from EPR at 5 K, and those that are obtained from theoretical simulation (see Tables S12 and S19 of the supplementary materials) are quite different, revealing the importance of the magnetic anisotropy in this model. We assume that the second data set is more reliable as it takes into account the reduced magnetic anisotropy at room temperature.

First Principle Calculations

Electronic Structure Calculations. The electronic structure of $[\text{Fe}^{\text{III}}(\text{Tp})(\text{CN})_3]^-$ was previously described by Ridier *et al.*¹⁴ and is therefore only briefly discussed here. Considering at first sight an octahedral environment around the Fe(III) ion, the scalar relativistic (SR) GS corresponds to a spin-doublet state ${}^2T_{2g}$ with formally an $t_{2g}^5 e_g^0$ electronic configuration (see Figure 5). However, the trigonal distortion in $[\text{Fe}^{\text{III}}(\text{Tp})(\text{CN})_3]^-$ lifts the degeneracy of the ${}^2T_{2g}$ state into two orbitally degenerate spin-doublet states 2E and into one non-degenerate 2A state. As seen in Table S10, the two 2E states are found to be the lowest in energy at the PT2-SR level and are separated from the excited state 2A by a large energy gap of ca. 2300 cm^{-1} . It is worth mentioning that the lowest spin-quartet and spin-sextet states are found at 9356 and 13747 cm^{-1} above the GS, respectively. Introduction of the spin-orbit coupling (SOC) does not drastically change the electronic structure. By symmetry, the SR 2E states are allowed to mix with each other and give rise to two Kramers doublets separated from each other by 628 cm^{-1} . The SOC barely affects the energies of the quartet and sextet states, which remain both extremely disfavored energetically.

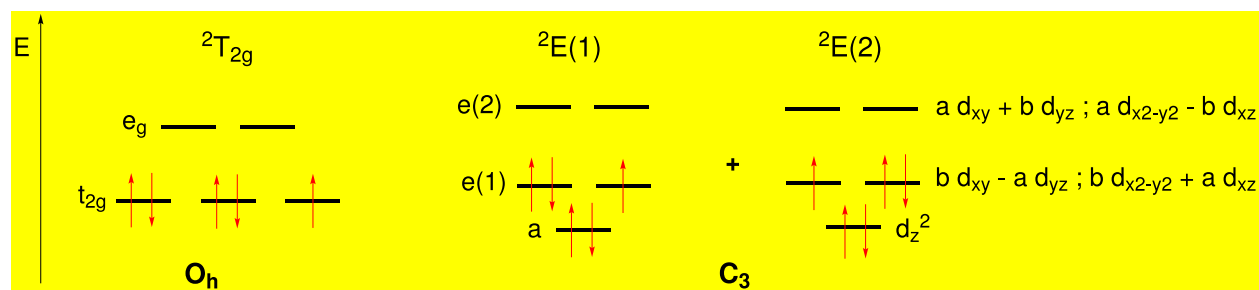


Figure 5. Schematic representation of the electronic configuration of the GS of $[\text{Fe}^{\text{III}}(\text{Tp})(\text{CN})_3]^-$ in the case of a perfectly octahedral complex (left, O_h) and for a distorted structure spanning the C_3 symmetry point group (right). The set of $e(2)$ orbitals correspond to the σ^* orbitals in Figure 7.

The natural orbitals (NOs) of the SO GS of $[\text{Fe}^{\text{III}}(\text{Tp})(\text{CN})_3]^-$ are shown in Figure S12 along with their occupation numbers. The largest occupation numbers (1.96 electron (e)) correspond to the NOs labeled σ . As already noted for transition metal complexes with cyanido ligands,^{111,112,113} the $3d$ metal-centered orbitals spanning the e irreducible representation (e_g in the parent O_h symmetry point group) can form a covalent bond of σ character with the $2p$ orbitals of the surrounding ligands. The bonding combination is formally doubly occupied whereas the

antibonding one (σ^*) is vacant. The non-integer occupation numbers of the σ and σ^* NOs reveal here the correlation effects that take place between these orbitals. As expected from Figure S12, the NO belonging to the a symmetry is found almost doubly occupied and corresponds to a $3dz^2$ orbital. Finally, the unpaired electron is distributed into the two non-bonding e orbitals. It is worth mentioning that in a strictly trigonal environment, the occupation of these two NOs would be equivalent and equal to 1.5 e. However, due to a slight symmetry breaking the occupation numbers are 1.66 and 1.30 e, respectively. This distribution corresponds to the mixing of the two SR electronic configurations 2E into the SO wavefunction as seen in Table S10.

Paramagnetic NMR Calculations. The isotropic ligand chemical shifts (δ^{calc}) for the ^{13}C and ^{15}N atoms of the cyanido ligands were calculated using Equation (7) and the principal results are shown in Figure 6. Additional data are given in Tables S17 and S18, while the calculated proton chemical shifts are given in Figure S16 of the SI. Considering the complexity of calculating properly ligand chemical shifts in paramagnetic complexes, the calculated data are overall found in satisfactory agreement with the experimental data. Indeed, the calculations were able to reproduce the sign of the experimental chemical shifts and the relative large magnitude between the ^{13}C and ^{15}N shifts. As shown in Figure 6, the calculated chemical shifts strongly depend on the values of the g -factors and HyFCCs used in Equation (7). The use of g -factors from the PT2-SO calculations leads to larger chemical shifts compared to the ones obtained at the DFT level. These results are consistent with the increase of the anisotropy factor (Δg) and isotropic values (g_{iso}) when using the PT2-SO results (see Table S13). Additionally, the use of the hybrid functionals B3LYP and PBE0 instead of the GGA functional PBE leads to an increase of the ^{13}C HyFCC and a decrease of the ^{15}N HyFCCs (see Table S14). Overall, at our best level of calculations, i.e. the use of the g -factors from the PT2-SO calculations in combination with the HyFCCs obtained at the PBE0/JCPL level, the averaged calculated chemical shifts for the ^{13}C and ^{15}N atoms are of -3836 and +875 ppm, respectively. These theoretical chemical shifts are in relatively good agreement with the experimental ones and tend to confirm the spin-density distribution observed experimentally.

A breakdown of the calculated chemical shifts in term of Fermi-contact and pseudo-contact contributions is given in Table 3. The reader is reminded that in these calculations no approximation is made in the spatial extension of the spin density for the calculations of the

hyperfine coupling constant A^{SD} , in opposition to the point-dipole approximation. This difference is expected to strongly impact the calculation of the pseudo-contact chemical shifts.¹¹⁴ For the ^{13}C atoms, the large paramagnetic shifts arise largely from a contact contribution with calculated δ^{FC} larger than 4500 ppm (for $T = 298\text{K}$). These contact contributions are only slightly counterbalanced by a small pseudo-contact contribution with opposite sign ($\delta^{PC} \approx -240$ ppm). The large FC term, in combination with the large isotropic HyFCCs calculated for the ^{13}C , suggests the presence of an important negative spin density at the carbon nuclei. On the other hand, the δ^{FC} contributions of the pNMR shift of the ^{15}N atoms strongly decrease in magnitude and are of opposite sign than those calculated for ^{13}C . This behavior is in good agreement with a positive spin density of smaller magnitude at the nitrogen nuclei, as observed experimentally. Interestingly, the pseudo-contact contributions are calculated larger for ^{15}N than for ^{13}C (see Table 3), despite the fact that the carbon atoms are closer to the paramagnetic center. Indeed, if one assumes a purely dipolar mechanism within a point-dipole approximation, the pseudo-contact term should decrease with a factor of $(1/r^3)$, as the C and N atoms exhibit similar polar angles with respect to the magnetic axis (see Equation (3)).

The difference in the FC / PC separation of the pNMR shifts between the ab-initio results and the point-dipole approximation results from the different definitions of the δ^{PC} term. In the ab-initio calculations, the magnitude of δ^{PC} is proportional to the anisotropic part of the Zeeman and hyperfine coupling matrices, and not only to the metal-ligand distance. Therefore, if the calculated isotropic HyFCCs for ^{13}C are much larger than those for ^{15}N , giving larger δ^{FC} contributions for the carbon atoms, on the other hand, the HyFCCs for ^{15}N are more anisotropic than those obtained for ^{13}C , leading to stronger δ^{PC} contributions for the nitrogen centers. This result could suggest that the spin density distribution at the nitrogen nuclei is less spherical than the spin density at the carbon nuclei.

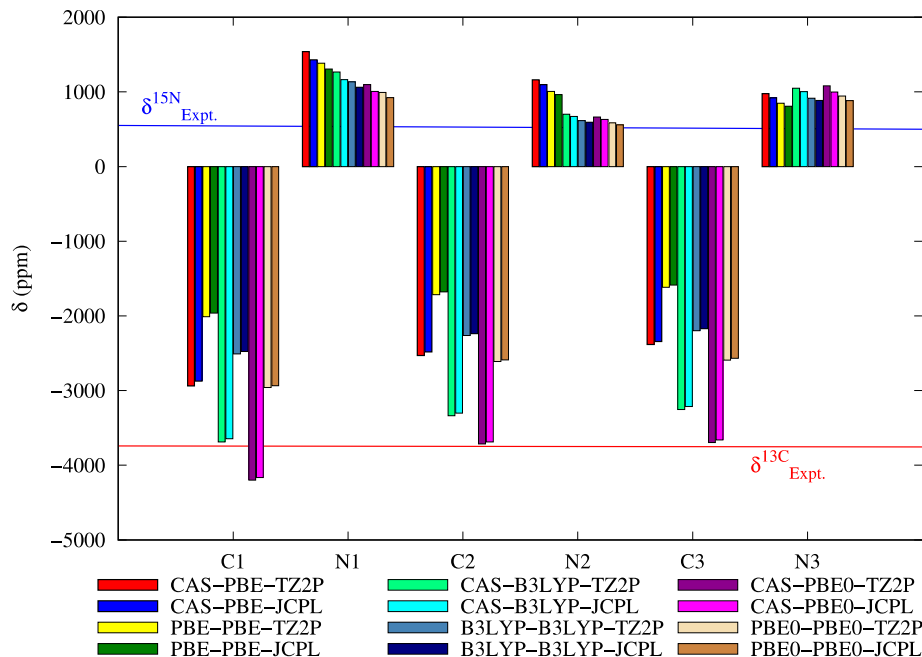


Figure 6. Calculated isotropic chemical shifts (δ^{calc} in ppm) for the ^{13}C and ^{15}N atoms of the cyanido ligands in $[\text{Fe}^{\text{III}}(\text{Tp})(\text{CN})_3]^-$ using Equation (10). The chemical shifts are given as a function of (i) the g -factors (CAS or KS-DFT results of Table S13), (ii) the functional used to calculate the HyFCCs (PBE, B3LYP and PBE0 results of Table S14), (iii) the basis set used to calculate the HyFCCs (TZ2P and JCPL results of Table S14). The averaged experimental chemical shifts (δ^{exp}) are also given for comparison ($T = 310$ K for nitrogen atoms and $T = 334$ K for carbon atoms).

Table 3. Calculated isotropic paramagnetic chemical shifts (δ^{pNMR}) for the ^{13}C and ^{15}N atoms of the cyanido ligands obtained using the PBE0/JCPL KS-DFT results for the HyFCCs and the PT2-SO results for the g -factors. A breakdown of δ^{pNMR} is given in term of Fermi-Contact (δ^{FC}) and Pseudo-Contact (δ^{PC}) contributions. For comparison, the calculated pseudo-contact shifts (δ^{PC}) using Equation (3) are given.^(a)

	δ^{pNMR}	δ^{FC}	δ^{PC}	$\delta^{\text{PC (b)}}$	$\delta^{\text{PC (c)}}$
C1	-4863	-5110	247	-10	-17
N1	1102	75	1027	-10	-10
C2	-4337	-4557	220	55	27
N2	702	47	654	6	1
C3	-4303	-4565	262	76	85
N3	1082	151	930	10	15

^a $T = 298$ K for nitrogen and carbon atoms for comparison with experimental data. ^b Using the PT2-SO g -factors in Equation (3) via Equation S9. ^c Using the calculated magnetic susceptibility in Equation (3).

Spin Density from First Principle Calculations. The spin magnetization ($m_z^S(\mathbf{r})$) along the z magnetic axis for the SO GS of $[\text{Fe}^{\text{III}}(\text{Tp})(\text{CN})_3]^-$ is shown in Figure 7. The reader is reminded that in the absence of the SOC, $m_z^S(\mathbf{r})$ corresponds to the usual spin density, and that the z magnetic axis in $[\text{Fe}^{\text{III}}(\text{Tp})(\text{CN})_3]^-$ is oriented along the Fe-B direction. The spin magnetization is principally localized on the iron center with a large blue density arising from the occupation of the partially filled $3d$ orbitals. The corresponding spin expectation value $\langle S_z \rangle = 0.48$ is close to the one expected for a SR spin-doublet with $M_S = 1/2$, confirming the small mixing with other spin states via SOC. Additionally, important negative magnetizations (i.e. the σ -type orange lobes in $m_z^S(\mathbf{r})$) are calculated on the carbon atoms of the CN ligands, whereas small positive spin magnetizations (i.e. the π -type blue lobes) are found on the nitrogen atoms. This pattern in $m_z^S(\mathbf{r})$ is characteristic of transition metal complexes with cyanido ligands,¹⁰² and can be rationalized by studying the natural spin orbitals (NSOs) and their spin populations. As seen in Figure 7, the non-bonding $3d$ NSOs of e symmetry have the largest positive spin populations, leading to the large positive magnetization on the metal center. Furthermore, these two NSOs exhibit little metal π -back donation (spin-delocalization) into the π^* orbitals of the CN ligands,^{113,115} which gives rise to the small positive magnetization on the nitrogen atoms. On the other hand, the small positive spin populations of the σ NSO and the equivalent negative spin populations in the σ^* , reveal the spin-polarization effect that takes place along the covalent Fe-C bonds and leads to a sizable σ -type negative spin magnetization on the carbon atoms. This distribution pattern of the spin-density is consistent with the ^{13}C and ^{15}N NMR measurements and confirmed by the PND analysis as detailed below.

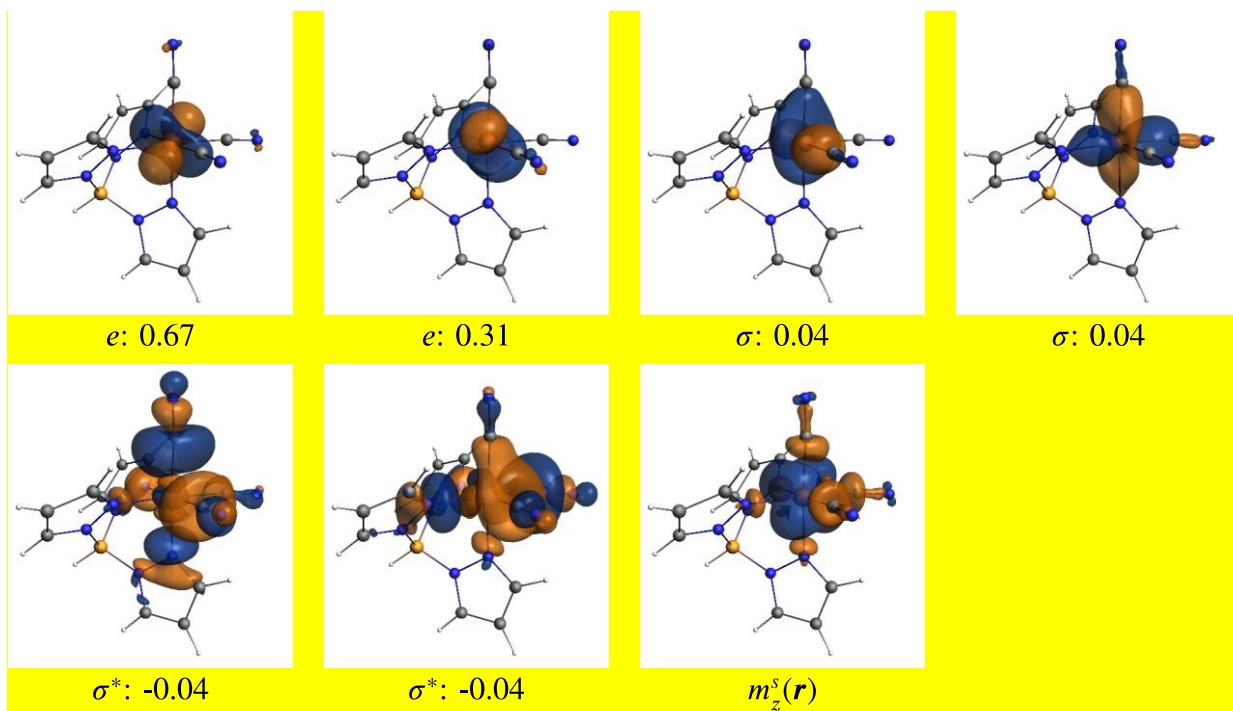


Figure 7. Selected natural spin orbitals (isosurface values = ± 0.03 au.; blue = positive and orange = negative) and their spin populations for the SO GS of $[\text{Fe}^{\text{III}}(\text{Tp})(\text{CN})_3]^-$ using the doublet component. The associated spin magnetization $m_z^S(r)$ is also given with isosurface values of ± 0.005 au. CAS(9,12)PT2-SO results.

The SR-ZORA spin density obtained with the PBE0 functional ($\rho^{\text{PBE0}}(r)$) is also shown in **Figure 8**, and the associated atomic spin densities are given in Table S11 for the different functionals used. The comparison with the SO spin magnetization reveals that KS-DFT calculations are able to reproduce properly the nature of the GS with a similar shape of the spin density at the iron center. Moreover, a similar pattern is also found on the cyanido ligands, but the magnitude of the spin-delocalization on the nitrogen atom, and the magnitude of the spin-polarization on the carbon atoms are much larger at the KS-DFT level than with CAS calculations. As shown in Figure S13 and in Table S11 of the SI, the use of different functionals does not strongly alter the distribution of the spin density. A slight decrease of the spin-delocalization on the nitrogen atoms is calculated when going from PBE to PBE0. This behavior is expected as the delocalization error inherent to KS-DFT calculations should decrease with the increase of percentage of exact exchange in the functional. On the other hand, the negative atomic spin density on the carbon atoms increases in magnitude when using hybrid functionals compared to the GGA functional. This increase of the spin-polarization can be further explained

by the increase of the ligand-to-metal σ donation from the CN^- ligands toward the Fe(III) ion. Indeed, the natural localized molecular orbitals (NLMOs) for each of the σ Fe-C bonds are depopulated in the α spin-NLMOs compared to the β spin-NLMOs (0.71 vs. 0.95 e with PBE0 in Figure S14), leaving an excess of β spin and hence, a large negative spin density.

Finally, a breakdown of the atomic spin density on the cyanido ligands in term of orbital contributions is given in Table S12 of the SI. Interestingly, the calculations give an averaged 2s spin density of -0.017 e on the carbon atoms, which is very close to the experimental value of -0.020 e (see Table 2) deduced from NMR measurements. On the other hand, the 2s spin density at the nitrogen nuclei is of +0.0006 e, much smaller than the +0.0030 e deduced from the NMR measurements, explaining the large differences in the Fermi-contact contributions. Interestingly, the spin density in the 2s orbital represent ca. 45 % of the total atomic spin density for the carbon atoms, whereas for the nitrogen ones it only represents 3 to 4 % of the atomic spin density. As visible in Figure 7, the spin density at the nitrogen atoms is mostly located in the 2p orbitals. This generates a large anisotropy in the HyFCCs of the ^{15}N , which could be responsible of the large deviations in the FC / PC separations compared to the deductions made from the experimental measurements.

Polarized Neutron Diffraction. Polarized neutron diffraction on a paramagnetic single crystal gives a direct access to the value of the induced magnetization density at each point of the crystal cell, a magnetic field being applied in order to align all the magnetic moments in the crystal. Therefore, this technique permits to access to the magnetization density distribution over the whole molecule in the case of a molecular crystal.

The experimental quantity measured by PND is the flipping ratio of each Bragg reflection, which is the ratio between the diffracted intensities I_{\uparrow} and I_{\downarrow} for an incident beam with vertical polarization, up and down respectively. It is related to the nuclear and magnetic structure factors. The flipping ratio measurement permits to determine the experimental magnetic structure factor $F_M(\vec{Q})$ for the Bragg peaks with scattering vector \vec{Q} , providing that the nuclear structure is known. Therefore PND gives an access to the magnetization density by Fourier summation of the F_M 's:

$$\rho(\vec{r}) = \frac{1}{V} \sum_{\vec{Q}}^{\infty} F_M(\vec{Q}) e^{-i\vec{Q}\vec{r}} \quad (12)$$

The magnetization density is the sum of the pure spin contribution and an orbital contribution mainly due to the 3d transition metal center, which has to be estimated in order to reach the pure spin density. However, as the Fourier summation is limited in the experiment to a finite number of Bragg peaks, the analysis of the experimental data is performed using a model for the spin density, the parameters of which are refined on the basis of the experimental data. In this model the spin density is written as the sum of independent atomic spin densities. For the atomic spin density located on the Fe atom, a 3d orbital model developed on d_{z^2} , $d_{x^2-y^2}$, d_{xz} , d_{yz} and d_{xy} basis functions was used. For the atoms of the ligands, spherical atomic densities were assumed.¹¹⁶

Spin Density from PND. In order to validate the spin density map drawn from the combination of the NMR measurements and of the theoretical calculations, polarized neutron diffraction measurements were performed at 2 K under a magnetic field of 5 Tesla on a single crystal of $\text{PPh}_4[\text{Fe}(\text{Tp})(\text{CN})_3]\cdot\text{H}_2\text{O}$ in order to have an experimental picture of the spin density in this complex. The results of the final PND data refinement are reported in Table S8 and the experimental spin populations, after normalization to 1, are compared to the one obtained from the SR KS-DFT calculations. The Fe spin population was refined together with four of the five a_i orbital coefficients of Equation (S8) (one coefficient must be fixed because of their relationship through the normalization condition) in addition to the C and N spin populations up to Fe second neighbors. A goodness of fit of 1.95 was obtained for the refinement of 20 parameters on the basis of 297 flipping ratios with $|R_{\text{obs}} - 1| > 3\sigma(R_{\text{obs}})$. The agreement factor on $|R - 1|$, i.e. on the difference of the flipping ratio to 1, is equal to 22.3 %. The experimental spin populations for Fe and for the C and N atoms, expressed in Bohr magnetons, are reported in first column of Table S8. For the Fe atom, the local induced magnetic moment is given by the sum of the orbit (0.42 μ_B) and spin (0.83 μ_B) populations. For all other atoms, the induced magnetic moments are equal to the experimental spin populations. The sum of the induced magnetic moments over the molecule is equal to 1.13 μ_B , and compares extremely well with the calculated magnetic moment of 1.125 μ_B (see Figure S14) obtained at the PT2-SO level. This value is, however, slightly smaller than the magnetization equal to 1.38 μ_B , in the experimental conditions of the PND experiment, i.e. at 2K under an applied field of 6T parallel to the c^* axis (see Figure S11). The normalized pure spin populations reported in Figure 8 caption and in second column of Table S8 were obtained after normalization to 1 unpaired electron per molecule. These normalized spin

populations compare extremely well with the spin populations obtained at the KS-DFT level. Additionally, a plot of the experimental spin density is shown in Figure 8 and can be directly compared with the theoretical plots. In both cases, one can observe a strong spin-polarization mechanism on the carbon atoms of the cyanido ligands and a less intense spin-delocalization mechanism on the nitrogen atoms.

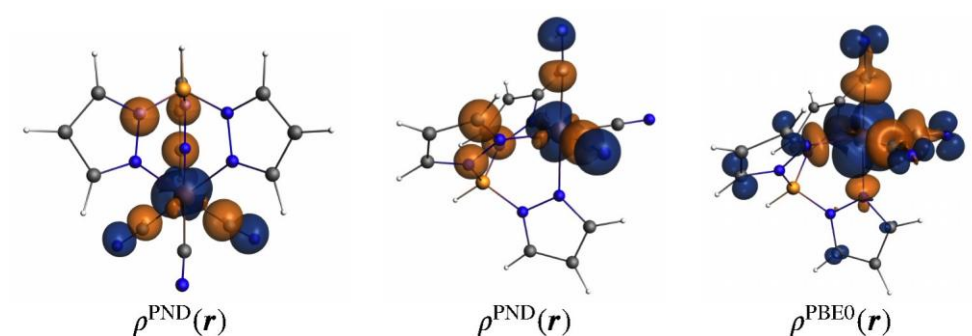


Figure 8. (left and middle) Plots of isosurface of the spin density determined by PND ($\rho^{\text{PND}}(r)$) and obtained by integration along the x direction of the local coordinate system. Isosurface values = ± 0.01 au. Only the experimental spin densities with magnitudes larger than the error bar are depicted. Normalized spin population (e): Fe = 1.251(38); C1 = -0.089(58); C2 = -0.063(72); C3 = -0.117(69); N1 = 0.075(54); N2 = 0.020(58); N3 = 0.110(52). (right) Additionally, the KS-DFT spin density ($\rho^{\text{PBE0}}(r)$) obtained with the functional PBE0 is shown for comparison. isosurface values of ± 0.005 au.

DISCUSSION

In this paper, we report the first combined experimental and theoretical study that uses NMR spectroscopy, PND analysis and ab-initio calculations to firmly probe the spatial distribution of the spin density in a paramagnetic compound, namely the [Fe^{III}(Tp)(CN)₃]⁻ building block. Each experimental technique has its own specificities and shows pros and cons. While PND is a direct technique that gives access to a map of the magnetization density in the crystal cell, and therefore to the magnetic moment on the paramagnetic metal center, NMR provides an indirect access to the spin density delocalized on the coordinating ligands. Additionally, the sensitivities of the two techniques are quite different. NMR spectroscopy is extremely sensitive to small amounts of spin density localized on remote position of the ligands, in particular on protons. For example, a contact term of 10 ppm in the proton spectra of an Fe(III) low-spin species such as

the $[\text{Fe}^{\text{III}}(\text{Tp})(\text{CN})_3]^-$ corresponds to a spin density of $0.000045 \text{ a.u.}^{-3}$. The main experimental limitation, however, arises from the fast nuclear magnetic relaxation in presence of unpaired electrons. This leads to broad or undetectable NMR signals, in particular for those atoms, which bear important amount of spin density (such as the metal ion). On the contrary, PND is more sensitive to high amount of magnetization density. It thus allows probing the local magnetization onto the paramagnetic center, but gives only rough estimates of the magnetization extension on the coordination sphere atoms, in particular the donor atoms. The main experimental limitations here come from the use of heavy instruments and the need of large single crystals. Overall, NMR and PND techniques lead to experimental pictures of the spin density distribution that are not directly comparable, but which can be connected with the help of quantum chemistry analysis such as a combination of KS-DFT and multi-reference calculations.

Table 5. Summary of the spin density information collected in this work. $\rho^{\square\square\square\square\square\square}(s)$ and $\rho^{\square\square\square\square\square\square}(s)$ correspond to the spin population on i^{th} s orbital determined from NMR measurements and KS-DFT (PBE0/JCPL) calculation, respectively. $\rho^{\square\square\square\square\square\square}(\mathbf{r})$ and $\rho^{\square\square\square\square\square\square}(\mathbf{r})$ correspond to the total atomic spin population determined from KS-DFT (PBE0/JCPL) calculation and PND analysis, respectively.

	Fe	C	N	H ₃	H ₄	H ₅	BH
$\rho^{\square\square\square\square\square\square}(s)$	-	-0.020 / -0.020	0.002 / 0.003	$-72.0 \cdot 10^{-6}$	$-41.7 \cdot 10^{-6}$	$-94.4 \cdot 10^{-6}$	$-80.0 \cdot 10^{-6}$
$\rho^{\square\square\square\square\square\square}(s)$		-0.016 / -0.018	0.000 / 0.001	$-360 \cdot 10^{-6}$	$-90 \cdot 10^{-6}$	$-360 \cdot 10^{-6}$	$40 \cdot 10^{-5}$
$\rho^{\square\square\square\square\square\square}(\mathbf{r})$	1.040	-0.034 / -0.047	0.009 / 0.027	$-360 \cdot 10^{-6}$	$-90 \cdot 10^{-6}$	$-360 \cdot 10^{-6}$	$40 \cdot 10^{-5}$
$\rho^{\square\square\square\square\square\square}(\mathbf{r})$	1.251	-0.063 / -0.117	0.020 / 0.110	-	-	-	-

A summary of the spin density information collected in this manuscript is given in Table 5. Both PND analysis and theoretical calculations revealed a large and positive spin density localized on the iron center, and principally distributed in the non-bonding 3d orbitals of formally t_{2g} symmetry (assuming O_h symmetry). Additionally, a strong spin-polarization mechanism of the spin density was highlighted for the carbon atoms of the cyanido ligands resulting from a strong σ -type donation to the iron ion. On the other hand, positive spin densities were also characterized on the nitrogen atoms of the cyanido ligands. In that case, the spin-density arises from a spin-delocalization mechanism via a metal π -back donation into the π^* orbitals of the CN ligands.

This spatial distribution of the spin density was confirmed by NMR measurements. The orbital spin density values extracted from the NMR analyses were found in qualitative agreement with those obtained from PND and ab-initio calculations: both techniques converging on the sign and on the C/N relative amount of spin density. Additionally, the spin-polarization of the Fe-C bonds was found responsible for the strongly axial ^{13}C CSA tensor. In contrast the low symmetry of the ^{15}N CSA tensor reflects the anisotropic distribution of the spin density at these nuclei due to the spin-delocalization in the $2p$ orbitals of the nitrogen atoms.

Although NMR is very powerful at detecting small amount of spin density onto ligand's atoms, extraction of magnetic information from experimental chemical shifts is indirect and relies on different approximations. The most important challenge lies in the correct estimation of the pseudo-contact contribution. Different experimental approaches were previously explored in the literature. For instance, in the case of metalloproteins the paramagnetic shift of protons located at remote positions of a paramagnetic metal center can be assumed of pure dipolar origin, i.e. $\delta^{\text{pNMR}} = \delta^{\text{PC}}$.^{107,110} Therefore, knowing the position and the paramagnetic shift of a set of protons allows extracting the magnetic anisotropy parameters, and then calculating δ^{PC} of any protons of the compound.¹¹⁷ The situation is more complicated in small paramagnetic complexes but alternative methods were proposed. For example, *Knorr et coll.* used the quadrupolar splitting of ^2H nuclei to access to local anisotropy of the susceptibility which governs the pseudo-contact term.¹¹⁸ This approach limited to the measurement of spin density at protons, requires to synthesize and to study deuterated samples. Another experimental approach is based on the substitution of protons on the ligands by methyl groups.¹⁰⁸ The comparison of the ^1H chemical shift of the protons and their methylated counterpart allows extracting an estimate of δ^{PC} . However, this approach also suffers from approximation, as the ligand substitution can influence the electronic properties of the complexes (*eg.* through inductive effect) and thus it can alter the spin density distribution.

In this work, we have tested the point-dipole approximation, which is the most popular approach for the extraction of the δ^{PC} contribution of paramagnetic shifts. The comparison of our experimental results with ab-initio calculations permits to underline different limitations of the point-dipole model, which differ with the nature of the probed nuclei. While theoretical calculations reproduce well the ^{13}C and ^{15}N experimental chemical shift, the relative proportion of the Fermi-contact term and of the pseudo contact term shows some apparent discrepancies in

comparison with the values deduced from the NMR data (Table 6). The use of the point-dipole model, *ie.* considering that the spin-density is only located on the paramagnetic center, leads to small value of the pseudo-contact terms. This suggests that both ^{13}C and ^{15}N pNMR shifts resulted from a strong Fermi-contact contribution that would be due to a sizable spin-density located in the 2s orbitals of these ligands. The ab-initio results, which do not approximate the spatial distribution of the spin-density, confirmed the amount of spin-density at the carbon nuclei, and hence, the large Fermi-contact term for the ^{13}C pNMR shifts. However, for the nitrogen nuclei, the calculated atomic spin-densities were found principally in localized 2p orbitals and not in the core 2s orbitals. This spin-density distribution led to a very small FC contribution and a large PC term in opposition to the NMR deductions. This large discrepancy between the two separation methods allows underlining a weakness of the point-dipole model: When the spin-density is distributed in both ligand *s* and *p* orbitals of the probed nuclei, the point-dipole approach underestimates the pseudo-contact shift due to an overestimation of the spin-density located in *s* orbitals.

Table 6. Summary of the experimental (Expt.) and calculated (Calc.) pseudo-contact (δ^{PC}) and Fermi-contact (δ^{FC}) contributions (in ppm) to the pNMR shifts for the ^{13}C and ^{15}N atoms of the cyanido ligands and the ^1H of the Tp ligand. All the values are reported for $T = 298\text{ K}$.

	^{13}C	^{15}N	H ₃	H ₄	H ₅	BH
$\delta_{\text{Expt.}}^{\text{PC}}$ (a)	-11.6 / +36.5	-9.9 / +7.3	-60.7	-4.60	13.9	64.8
$\delta_{\text{Expt.}}^{\text{PC}}$ (b)	-8.6 / + 27.0	-7.4 / +5.4	-44.9	-3.40	10.3	47.8
$\delta_{\text{Expt.}}^{\text{FC}}$ (a)	-4390 / -4309	569 / 636	1.27	-7.73	-24.2	-35.2
$\delta_{\text{Expt.}}^{\text{FC}}$ (b)	-4380 / -4312	570 / 633	-14.6	-8.93	-20.6	-18.2
$\delta_{\text{Calc.}}^{\text{PC}}$	220 / 262	654 / 1026	-14	-17	-3	29
$\delta_{\text{Calc.}}^{\text{FC}}$	-4557 / -5110	47 / 151	-23	-20	-23	3

(a) Estimated using g_{ii} value obtained by EPR measurements at 5K. (b) Estimated using g_{ii} value deduced from the calculated magnetic susceptibility at 298 K.

We additionally looked at the ^1H paramagnetic NMR shifts of the Tp ligands, which should principally arise from the pseudo-contact contribution, as only small amount of spin-density should be present at the proton nuclei. Overall, the calculated paramagnetic shifts are in relatively good agreement with the NMR measurements, and the sign and the relative magnitude

of the spin-density localized in the $1s$ orbitals of the protons are almost consistent between the ab-initio results and the experimental values (see Table 5). However, the two separation methods still lead to some discrepancy (see Table 6). In particular, the point-dipole approximation produces much larger δ^{PC} contributions than those calculated from first principle calculations. Such deviations highlight the importance of using the proper magnetic anisotropy tensor for estimating the pseudo-contact contribution within the point-dipole model (Equations 3 and 4) for proton NMR shifts. Indeed, the large magnetic anisotropy in $[\text{Fe}^{\text{III}}(\text{Tp})(\text{CN})_3]^-$ characterized by EPR measurements at 5 K is strongly reduced at the temperature of the NMR **measurements**. As shown in Table 6, the use of the magnetic anisotropy tensor deduced from the calculated χT at room temperature strongly improves the agreement between the experimentally deduced and the calculated δ^{PC} contributions.

CONCLUSION

The unprecedented application of three key methods, Polarized Neutron Diffraction (PND), paramagnetic NMR spectroscopy (pNMR) and ab-initio calculations, to the study of a building block for assembling magnetic materials, $[\text{Fe}^{\text{III}}(\text{Tp})(\text{CN})_3]^-$, yields a detailed map of the spin density distribution at the atomic scale. The advantage of using ^{13}C and ^{15}N solid-state and ^1H solution pNMR is that it detects very small amounts of spin density at the ligand atoms, whereas PND is well suited to characterize the spin density located at the paramagnetic metal center and, less precisely, at the cyanido ligands. The two techniques give experimental pictures of the magnetism at the local scale, which are not directly comparable, but are then connected with the help of quantum chemistry analysis, leading to very complementary views.

The characterization of a clear and detailed spin density map is of particular interest to unveil the mechanisms transferring the spin density from the metal to notably the CN ligands, which would serve as links to other building blocks in prospective magnetic materials. It is also important for the rationalization of the paramagnetic NMR chemical shift and for the estimation of the pseudo-contact and contact contributions. In particular, the combined experimental and theoretical approach has allowed underlining the limitation of the point-dipole model, which is commonly used to extract spin density through NMR. **Our study showed that the use of g tensors obtained at**

low temperature in the electronic ground state may lead to over-estimate of the pseudo contact term. Significantly improved results can be obtained by estimated the reduced magnetic anisotropy at room temperature. In follow-up work we aim for applying such investigations to a wider range of systems in order to more generally evaluate the methods for singling out the pseudo-contact contribution to the pNMR shifts.

ACKNOWLEDGMENTS

We are grateful to the CNRS, “Ministère de l’Enseignement et de la Recherche” for their financial support. FG and BLG acknowledge support from the European Research Council under the European Union’s Horizon 2020 research and innovation program (ERC-CoG MULTIPROSMM, Grant agreement 7255184). FG, KC and BLG thank the French GENCI/IDRIS-CINES centers for high-performance computing resources (allocations A0020800649 and A0040800649).

SUPPORTING INFORMATION

Additional data regarding the experimental and computational details, experimental NMR for the diamagnetic reference and the paramagnetic complex, crystal structure data for the diamagnetic reference and the magnetization characterization. DFT spin-densities, NLMOs, *g*-Factors and HyFCCs for $[\text{Fe}^{\text{III}}(\text{Tp})(\text{CN})_3]^-$. Additional calculated NMR shielding constants and chemical shifts. X-ray crystallographic files in CIF format of $\text{PPh}_4[\text{Co}(\text{Tp}^*)(\text{CN})_3]^- \text{CH}_3\text{CN}$ are available from the Cambridge Crystallographic Data Centre, 12 Union road, Cambridge CB2 1EZ, UK (fax: +44-1223-336033; email: deposit@ccdc.cam.ac.uk or www: <http://www.ccdc.cam.ac.uk>) on request, on quoting the deposition number CCDC 1912048.

TABLE OF CONTENTS GRAPHICS

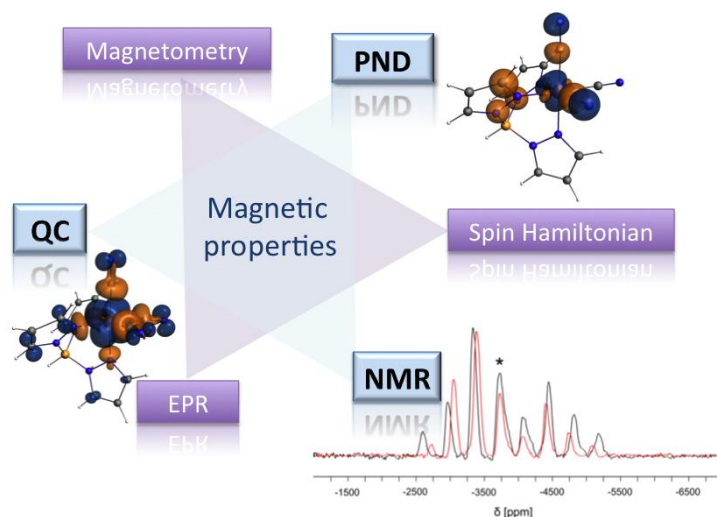


TABLE OF CONTENTS SYNOPSIS

The spin-density distribution in the molecular building block $[\text{Fe}^{\text{III}}(\text{Tp})(\text{CN})_3]^-$ is deeply understood by using polarized neutron diffraction, paramagnetic nuclear magnetic resonance spectroscopy and quantum chemistry calculations.

DEDICATION

This article is dedicated to Dr. Jean-François Halet on the occasion of his 60th birthday.

REFERENCES

¹ Ferrando-Soria, J.; Vallejo, J.; Castellano, M.; Martínez-Lillo, J.; Pardo, E.; Cano, J.; Castro, I.; Lloret, F.; Ruiz-García, R.; Julve, M. Molecular Magnetism, Quo Vadis? A Historical Perspective from a Coordination Chemist Viewpoint. *Coord. Chem. Rev.* **2017**, *339*, 17–103.

² Sessoli, R.; Gatteschi, D.; Caneschi, A.; Novak, M. A. Magnetic Bistability in a Metal-Ion Cluster. *Nature* **1993**, *365*, 141-143.

³ Winpenny, R. *Single-Molecule Magnets and Related Phenomena*. In *Structure and Bonding*. Springer-Verlag: Berlin/Heidelberg, **2006**; Vol. 122.

⁴ Gao, S. *Molecular Nanomagnets and Related Phenomena*. In *Structure and Bonding*. Springer Berlin Heidelberg: Berlin, Heidelberg, **2015**; Vol. 164.

⁵ Jafri, S. F.; Koumoussi, E. S.; Arrio, M.-A.; Juhin, A.; Mitcov, D.; Rouzière, M.; Dechambenoit, P.; Li, D.; Otero, E.; Wilhem, F.; Rogalev, A.; Joly, L.; Kappler, J.-P.; Cartier dit Moulin, C.; Mathonière, C.; Clérac, R.; Sainctavit, P. Atomic Scale Evidence of the Switching Mechanism in a Photomagnetic CoFe Dinuclear Prussian Blue Analogue. *J. Am. Chem. Soc.* **2019**, *141*, 3470–3479.

⁶ Shatruk, M.; Avendano, C.; Dunbar, K. R. Cyanido-Bridged Complexes of Transition Metals: A Molecular Magnetism Perspective. In *Progress in Inorganic Chemistry*; Karlin, K. D., Ed.; John Wiley & Sons, Inc.: Hoboken, NJ, USA, **2009**; pp 155–334.

⁷ Lescouëzec, R.; Toma, L. M.; Vaissermann, J.; Verdaguer, M.; Delgado, F. S.; Ruiz-Pérez, C.; Lloret, F.; Julve, M. Design of Single Chain Magnets through Cyanido-Bearing Six-Coordinate Complexes. *Coord. Chem. Rev.* **2005**, *249*, 2691–2729.

⁸ Lescouëzec, R.; Vaissermann, J.; Lloret, F.; Julve, M.; Verdaguer, M. Ferromagnetic Coupling between Low- and High-Spin Iron(III) Ions in the Tetranuclear Complex *fac*-{[Fe^{III}{HB(Pz)₃}(CN)₂(μ-CN)]₃Fe^{III}(H₂O)₃}·6H₂O ([HB(Pz)₃][−]=Hydrotris(1-Pyrazolyl)Borate). *Inorg. Chem.* **2002**, *41*, 5943–5945.

⁹ Ferko, P.; Holmes, S. Pyrazolylborate Cyanometalate Single-Molecule Magnets. *Curr. Inorg. Chem.* **2013**, *3*, 172–193.

¹⁰ Liu, T.; Dong, D.-P.; Kanegawa, S.; Kang, S.; Sato, O.; Shiota, Y.; Yoshizawa, K.; Hayami, S.; Wu, S.; He, C.; et al. Reversible Electron Transfer in a Linear {Fe₂Co} Trinuclear Complex Induced by Thermal Treatment and Photoirradiation. *Angew. Chem. Int. Ed.* **2012**, *124*, 4443–4446.

¹¹ Jiménez, J.-R.; Sugahara, A.; Okubo, M.; Yamada, A.; Chamoreau, L.-M.; Lisnard, L.; Lescouëzec, R. A [Fe^{III}(Tp)(CN)₃][−] Scorpionate-Based Complex as a Building Block for Designing Ion Storage Hosts (Tp: Hydrotrispyrazolylborate). *Chem. Commun.* **2018**, *54*, 5189–5192.

¹² Hoshino, N.; Iijima, F.; Newton, G. N.; Yoshida, N.; Shiga, T.; Nojiri, H.; Nakao, A.; Kumai, R.; Murakami, Y.; Oshio, H. Three-Way Switching in a Cyanido-Bridged [CoFe] Chain. *Nature Chem.* **2012**, *4*, 921–926.

¹³ Koumoussi, E. S.; Jeon, I.-R.; Gao, Q.; Dechambenoit, P.; Woodruff, D. N.; Merzeau, P.; Buisson, L.; Jia, X.; Li, D.; Volatron, F.; Mathonière, C.; Clérac, R. Metal-to-Metal Electron

Transfer in Co/Fe Prussian Blue Molecular Analogues: The Ultimate Miniaturization. *J. Am. Chem. Soc.* **2014**, *136*, 15461–15464.

¹⁴ Ridier, K.; Mondal, A.; Boilleau, C.; Cador, O.; Gillon, B.; Chaboussant, G.; Le Guennic, B.; Costuas, K.; Lescouëzec, R. Polarized Neutron Diffraction to Probe Local Magnetic Anisotropy of a Low-Spin Fe(III) Complex. *Angew. Chem. Int. Ed.* **2016**, *55*, 3963–3967.

¹⁵ Kahn, O. *Molecular Magnetism*. Wiley-VCH, New York, **1993**.

¹⁶ Bar, A. K.; Pichon, C.; Sutter, J.-P. Magnetic Anisotropy in two- to Eight-Coordinated Transition-Metal Complexes: Recent Developments in Molecular Magnetism. *Coord. Chem. Rev.* **2016**, *308*, 346–380.

¹⁷ Roessler, M. M.; Salvadori, E. Principles and Applications of EPR Spectroscopy in the Chemical Sciences. *Chem. Soc. Rev.* **2018**, *47*, 2534.

¹⁸ Corradini, V.; Moro, F.; Biagi, R.; del Pennino, U.; De Renzi, V.; Carretta, S.; Santini, P.; Affronte, M.; Cezar, J. C.; Timco, G.; Winpenny, R. E. P. X-Ray Magnetic Circular Dichroism Investigation of Spin and Orbital Moments in Cr₈ and Cr₇Ni Antiferromagnetic Rings. *Phys. Rev. B* **2008**, *77*, 014402.

¹⁹ Day, P.; Delfs, C. D.; Figgis, B. N.; Reynolds, P. A.; Tasset, F. Polarized Neutron Diffraction from Cs₂KFe(CN)₆: The Orbital Moment and Its Anisotropy. *Mol. Phys.* **1993**, *78*, 769–780.

²⁰ Figgis, B. N.; Kucharski, E. S.; Vrtis, M. Spin and Charge Transfer through Hydrogen Bonding in [Co(NH₃)₅(OH₂)] [Cr(CN)₆]. *J. Am. Chem. Soc.* **1993**, *115*, 176–181.

²¹ Figgis, B. N.; Forsyth, J. B.; Reynolds, P. A. Spin Density of the Hexacyanochromate(III) Ion Measured by Polarized Neutron Diffraction. *Inorg. Chem.* **1987**, *26*, 101–105.

²² Craven, M.; Nygaard, M. H.; Zadrozny, J. M.; Long, J. R.; Overgaard, J. Determination of d-Orbital Populations in a Cobalt(II) Single-Molecule Magnet Using Single-Crystal X-Ray Diffraction. *Inorg. Chem.* **2018**, *57*, 6913–6920.

²³ Thomsen, M. K.; Nyvang, A.; Walsh, J. P. S.; Bunting, P. C.; Long, J. R.; Neese, F.; Atanasov, M.; Genoni, A.; Overgaard, J. Insights into Single-Molecule-Magnet Behavior from the Experimental Electron Density of Linear Two-Coordinate Iron Complexes. *Inorg. Chem.* **2019**, *58*, 3211–3218.

²⁴ Suturina, E. A.; Mason, K.; Geraldes, C. F. G. C.; Kuprov, I.; Parker, D. Beyond Bleaney's Theory: Experimental and Theoretical Analysis of Periodic Trends in Lanthanide-Induced Chemical Shift. *Angew. Chem. Int. Ed.* **2017**, *56*, 12215–12218.

²⁵ Vonci, M.; Mason, K.; Suturina, E. A.; Frawley, A. T.; Worswick, S. G.; Kuprov, I.; Parker, D.; McIlhnes, E. J. L.; Chilton, N. F. Rationalization of Anomalous Pseudocontact Shifts and

Their Solvent Dependence in a Series of C₃-Symmetric Lanthanide Complexes. *J. Am. Chem. Soc.* **2017**, *139*, 14166-14172.

²⁶ Castro, G.; Regueiro-Figueroa, M.; Esteban-Gómez, D.; Pérez-Lourido, P.; Platas-Iglesias, C.; Valencia, L. Magnetic Anisotropies in Rhombic Lanthanide(III) Complexes Do Not Conform to Bleaney's Theory. *Inorg. Chem.* **2016**, *55*, 3490-3497.

²⁷ Pell, A. J.; Pintacuda, G.; Grey, C. P. Paramagnetic NMR in solution and the Solid State. *Prog. Nucl. Magn. Reson. Spectrosc.* **2019**, *111*, 1-271.

²⁸ Grey, C. P.; Dupré, N. NMR Studies of Cathode Materials for Lithium-Ion Rechargeable Batteries. *Chem. Rev.* **2004**, *104*, 4493-4512.

²⁹ Mondal, A.; Gaultois, M. W.; Pell, A. J.; Iannuzzi, M.; Grey, C. P.; Hutter, J. and Kaupp, M. Large-Scale Computation of Nuclear Magnetic Resonance Shifts for Paramagnetic Solids Using CP2K. *J. Chem. Theory Comput.* **2018**, *14*, 377-394.

³⁰ Kim, J.; Middlemiss, D. S.; Chernova, N. A.; Zhu, B. Y. X., Masquelier, C.; Grey, C. P. Linking Local Environments and Hyperfine Shifts: A Combined Experimental and Theoretical ³¹P and ⁷Li Solid-State NMR Study of Paramagnetic Fe(II) Phosphates. *J. Am. Chem. Soc.* **2010**, *132*, 16825-16840.

³¹ Baumgärtel, N.; Flambard, A.; Köhler, F. H.; Lescouëzec, R. Paramagnetic Hexacyanometalates. The Diversity of Spin Distribution Studied by ¹³C and ¹⁵N MAS NMR Spectroscopy. *Inorg. Chem.* **2013**, *52*, 12634-12644.

³² Flambard, A.; Köhler, F. H.; Lescouëzec, R.; Revel, B. Probing Spin Density and Local Structure in the Prussian Blue Analogues CsCd[Fe/Co(CN)₆]·0.5H₂O and Cd₃[Fe/Co(CN)₆]₂·15 H₂O with Solid-State MAS NMR Spectroscopy. *Chem. Eur. J.* **2011**, *17*, 11567-11575.

³³ Flambard, A.; Köhler, F. H.; Lescouëzec, R. Revisiting Prussian Blue Analogues with Solid-State MAS NMR Spectroscopy: Spin Density and Local Structure in [Cd₃{Fe(CN)₆]₂]·15H₂O. *Angew. Chem. Int. Ed.* **2009**, *48*, 1673-1676.

³⁴ Trofimenko, S. Recent Advances in Poly(Pyrazolyl)Borate (Scorpionate) Chemistry. *Chem. Rev.* **1993**, *93*, 943-980.

³⁵ Lescouëzec, R.; Vaissermann, J.; Lloret, F.; Julve, M.; Verdaguer, M. Ferromagnetic Coupling between Low- and High-Spin Iron(III) Ions in the Tetranuclear Complex *fac*-{[Fe^{III}{HB(Pz)₃}(CN)₂(μ-CN)]₃Fe^{III}(H₂O)₃}·6H₂O ([HB(Pz)₃]⁻=Hydrotris(1-Pyrazolyl)Borate). *Inorg. Chem.* **2002**, *41*, 5943-5945.

³⁶ Mehring, M. *Principles of High Resolution NMR in Solids*; Springer-Verlag Berlin and Heidelberg, **1983**.

-
- ³⁷ Haeberlen, U. *Advances in Magnetic Resonance*; Waugh, J. Academic Press: New York, **1976**; Vol. 8.
- ³⁸ Earl, W. L.; Vanderhart, D. L. Measurement of ¹³C Chemical Shifts in Solids. *J. Magn. Reson. (1969)* **1982**, *48*, 35–54.
- ³⁹ Morcombe, C. R.; Zilm, K. W. Chemical Shift Referencing in MAS Solid State NMR. *J. Magn. Reson.* **2003**, *162*, 479–486.
- ⁴⁰ Hayashi, S.; Hayamizu, K. Chemical Shift Standards in High-Resolution Solid-State NMR (2) ¹⁵N Nuclei. *Bull. Chem. Soc. Japan* **1991**, *64*, 688–690.
- ⁴¹ Heise, H.; Köhler, F. H.; Xie, X. Solid-State NMR Spectroscopy of Paramagnetic Metallocenes. *J. Magn. Reson.* **2001**, *150*, 198–206.
- ⁴² Köhler, F. H.; Xie, X. Vanadocene as a Temperature Standard For ¹³C and ¹H MAS NMR and for Solution-State NMR Spectroscopy. *Magn. Reson. Chem.* **1997**, *35*, 487–492.
- ⁴³ te Velde, G.; Bickelhaupt, F. M.; Baerends, E. J.; van Gisbergen, S. J. A.; Fonseca Guerra, C.; Snijders, J. G.; Ziegler, T. Chemistry with ADF. *J. Comput. Chem.* **2001**, *22*, 931-967.
- ⁴⁴ Fonseca Guerra, C.; Snijders, J. G.; te Velde, G.; Baerends, E. J. Towards an order-N DFT method. *Theor. Chem. Acc.* **1998**, *99*, 391.
- ⁴⁵ Baerends, E. J.; Ziegler, T.; Atkins, A. J.; Autschbach, J.; Bashford, D.; Baseggio, O.; Bérces, A.; Bickelhaupt, F. M.; Bo, C.; Boerritger, P. M.; Cavallo, L.; Daul, C.; Chong, D. P.; Chulhai, D. V.; Deng, L.; Dickson, R. M.; Dieterich, J. M.; Ellis, D. E.; van Faassen, M.; Ghysels, A.; Giammona, A.; van Gisbergen, S. J. A.; Goetz, A.; Götz, A. W.; Gusarov, S.; Harris, F. E.; van den Hoek, P.; Hu, Z.; Jacob, C. R.; Jacobsen, H.; Jensen, L.; Joubert, L.; Kaminski, J. W.; van Kessel, G.; König, C.; Kootstra, F.; Kovalenko, A.; Krykunov, M.; van Lenthe, E.; McCormack, D. A.; Michalak, A.; Mitoraj, M.; Mor-ton, S. M.; Neugebauer, J.; Nicu, V. P.; Noodleman, L.; Osinga, V. P.; Patchkovskii, S.; Pavanello, M.; Peeples, C. A.; Philipsen, P. H. T.; Post, D.; Pye, C. C.; Ramanantoan-ina, H.; Ramos, P.; Ravenek, W.; Rodríguez, J. I.; Ros, P.; Rüger, R.; Schipper, P. R. T.; Schlüns, D.; van Schoot, H.; Schreckenbach, G.; Seldenthuis, J. S.; Seth, M.; Snijders, J. G.; Solà, M.; M., S.; Swart, M.; Swerhone, D.; te Velde, G.; Tognetti, V.; Vernooijs, P.; Versluis, L.; Visscher, L.; Visser, O.; Wang, F.; Wesolowski, T. A.; van Wezenbeek, E. M.; Wiesenekker, G.; Wolff, S. K.; Woo, T. K.; Yakovlev, A. L. “ADF2017, SCM, Theoretical Chemistry, Vrije Universiteit, Amsterdam, The Netherlands, <https://www.scm.com>”, **2017**.
- ⁴⁶ van Lenthe, E.; Baerends, E. J.; Snijders, J. G. Relativistic Regular two-component Hamiltonians. *J. Chem. Phys.* **1993**, *99*, 4597-4610.
- ⁴⁷ Perdew, J. P.; Burke, K.; Ernzerhof, M. Generalized Gradient Approximation Made Simple. *Phys. Rev. Lett.* **1996**, *77*, 3865-3868.
- ⁴⁸ Perdew, J. P.; Burke, K.; Ernzerhof, M. Generalized Gradient Approximation Made Simple. *Phys. Rev. Lett.* **1997**, *78*, 1396.

-
- ⁴⁹ Lee, C.; Yang, W.; Parr, R. G. Development of the Colle-Salvetti correlation-energy formula into a functional of the electron density. *Phys. Rev. B* **1988**, *37*, 785–789.
- ⁵⁰ Becke, A. D. Density functional thermochemistry. III. The role of exact exchange. *J. Chem. Phys.* **1993**, *98*, 5648–5652.
- ⁵¹ Ernzerhof, M.; Scuseria, G. E. Assessment of the Perdew-Burke-Ernzerhof. *J. Chem. Phys.* **1999**, *110*, 5029–5036.
- ⁵² Adamo, C.; Barone, V. Toward reliable density functional methods without adjustable parameters: The PBE0 model. *J. Chem. Phys.* **1999**, *110*, 6158–6170.
- ⁵³ van Lenthe, E.; Baerends, E. J. Optimized Slater-type basis sets for the elements 1 – 118. *J. Comput. Chem.* **2003**, *24*, 1142–1156.
- ⁵⁴ Moncho, S.; Autschbach, J. *J. Chem. Theory Comput.* **2010**, *6*, 223–234.
- ⁵⁵ Glendening, E. D.; Landis, C. R.; Weinhold, F. NBO 6.0: Natural bond orbital analysis program. *J. Comput. Chem.* **2013**, *34*, 1429–1437.
- ⁵⁶ van Lenthe, E.; Wormer, P. E. S.; van der Avoird, A. Density functional calculations of molecular g-tensors in the zero order regular approximation for relativistic effects. *J. Chem. Phys.* **1997**, *107*, 2488–2498.
- ⁵⁷ van Lenthe, E.; van der Avoird, A.; Wormer, P. E. S. Density functional calculations of molecular hyperfine interactions in the zero order regular approximation for relativistic effects. *J. Chem. Phys.* **1998**, *108*, 4783–4796.
- ⁵⁸ Schreckenbach, G.; Ziegler, T. Calculation of NMR shielding tensors using gauge-including atomic orbitals and modern density functional theory. *J. Phys. Chem.* **1995**, *99*, 606–611.
- ⁵⁹ Autschbach, J.; Patchkovskii, S.; Pritchard, B. *J. Chem. Theory Comput.* **2011**, *7*, 2175–2188.
- ⁶⁰ Krykunov, M.; Ziegler, T.; van Lenthe, E. Implementation of a Hybrid DFT Method for Calculating NMR Shieldings Using Slater-Type Orbitals with Spin–Orbital Coupling Included. Applications to ¹⁸⁷Os, ¹⁹⁵Pt, and ¹³C in Heavy-Metal Complexes. *J. Phys. Chem. A* **2009**, *113*, 11495–11500.**
- ⁶¹ Aquilante, F.; Autschbach, J.; Carlson, R. K.; Chibotaru, L. F.; Delcey, M. G.; Vico, L. D.; Fdez. Galván, I.; Ferré, N.; Frutos, L. M.; Gagliardi, L.; Garavelli, M.; Giussani, A.; Hoyer, C. E.; Manni, G. L.; Lischka, H.; Ma, D.; Malmqvist, P.-Å.; Müller, T.; Nenov, A.; Olivucci, M.; Pedersen, T. B.; Peng, D.; Plasser, F.; Pritchard, B.; Reiher, M.; Rivalta, I.; Schapiro, I.; Segarra-Martí, J.; Stenrup, M.; Truhlar, D. G.; Ungur, L.; Valentini, A.; Vancoillie, S.; Veryazov, V.; Vysotskiy, V. P.; Weingart, O.; Zapata, F.; Lindh, R. *J. Comput. Chem.* **2016**, *37*, 506–541.
- ⁶² Roos, B. O.; Taylor, P. R.; Siegbahn, P. E. M. A Complete Active Space SCF Method (CASSCF) using a Density Matrix Formulated Super-CI Approach. *Chem. Phys.* **1980**, *48*, 157–173.

-
- ⁶³ Andersson, K.; Malmqvist, P.-Å.; Roos, B. O.; Sadlev, A. J.; Wolinski, K. Second-Order Perturbation Theory with a CASSCF Reference Function. *J. Phys. Chem.* **1990**, *94*, 5483–5488.
- ⁶⁴ Douglas, M.; Kroll, N. M. Quantum Electrodynamical Corrections to the Fine Structure of Helium. *Ann. Phys.* **1974**, *82*, 89-155.
- ⁶⁵ Hess, B. A. Applicability of the no-pair equation with free-particle projection operators to atomic and molecular structure calculations. *Phys. Rev. A* **1985**, *32*, 756-763.
- ⁶⁶ Hess, B. A. Relativistic electronic-structure calculations employing a two-component no-pair formalism with external-field projection operators. *Phys. Rev. A* **1986**, *33*, 3742-3748.
- ⁶⁷ Wolf, A.; Reiher, M.; Hess, B. A. The generalized Douglas-Kroll transformation. *J. Chem. Phys.* **2002**, *117*, 9215-9226.
- ⁶⁸ Widmark, P.-O.; Malmqvist, P.-Å.; Roos, B. O. Density-matrix averaged atomic natural orbital (ANO) basis-sets for correlated molecular wave-functions. I. First row atoms. *Theor. Chim. Acta* **1990**, *77*, 291–306.
- ⁶⁹ Roos, B. O.; Lindh, R.; Malmqvist, P.-Å.; Veryazov, V.; Widmark, P.-O. Main group atoms and dimers studied with a new relativistic ANO basis set. *J. Phys. Chem. A* **2004**, *108*, 2851–2858.
- ⁷⁰ Roos, B. O.; Lindh, R.; Malmqvist, P.-Å.; Veryazov, V.; Widmark, P.-O. New relativistic ANO basis sets for transition metal atoms. *J. Phys. Chem. A* **2005**, *109*, 6575.
- ⁷¹ (a) Ridier, K.; Mondal, A.; Boilleau, C.; Cador, O.; Gillon, B.; Chaboussant, G.; Le Guennic, B.; Costuas, K.; Lescouëzec, R. Polarized Neutron Diffraction to Probe Local Magnetic Anisotropy of a Low-Spin Fe(III) Complex. *Angew. Chem.* **2016**, *128*, 4031–4035. (b) Ridier, K.; Mondal, A.; Boilleau, C.; Cador, O.; Gillon, B.; Chaboussant, G.; Le Guennic, B.; Costuas, K.; Lescouëzec, R. Polarized Neutron Diffraction to Probe Local Magnetic Anisotropy of a Low-Spin Fe(III) Complex. *Angew. Chem. Int. Ed.* **2016**, *55*, 3963–3967
- ⁷² Bolvin H. d-d Spectrum and High-Spin / Low-Spin Competition in d6 Octahedral Coordination Compounds: Ab Initio Study of Potential Energy Curves. *Inorg. Chem.* **1998**, *102*, 7525-7534.
- ⁷³ Charron, G.; Malkin, E.; Rogez, G.; Batchelor, L. J.; Mazerat, S.; Guillot, R.; Guihèry, N.; Barra, A. L.; Mallah, T.; Bolvin, H. Unraveling σ and π Effects on Magnetic Anisotropy in cis-NiA₄B₂ Complexes: Magnetization, HF-HFEPR Studies, First-Principles Calculations, and Orbital Modeling. *Chem. Eur. J.* **2017**, *22*, 1-14.
- ⁷⁴ Tsitovich, P. B.; Gendron, F.; Nazarenko, A. Y.; Livesay, B. N.; Lopez, A. P.; Shores, M. P.; Autschbach, J.; Morrow, J. R. Low-Spin Fe(III) Macrocyclic Complexes of Imidazole-Appended 1,4,7-Triazacyclononane as Paramagnetic Probes. *Inorg. Chem.* **2018**, *57*, 8364-8374.
- ⁷⁵ Malmqvist, P.-A.; Roos, B. O.; Schimmelpfennig, B. The restricted active space (RAS) state interaction approach with spin-orbit coupling. *Chem. Phys. Lett.* **2002**, *357*, 230-240.

-
- ⁷⁶ Bolvin, H. An Alternative Approach to the g-Matrix: Theory and Applications. *ChemPhysChem* **2006**, *7*, 1575-1589.
- ⁷⁷ Chibotaru, L. F.; Ungur, L. Ab initio calculation of anisotropic magnetic properties of complexes. I. Unique definition of pseudospin Hamiltonians and their derivation. *J. Chem. Phys.* **2012**, *137*, 064112-22.
- ⁷⁸ Gendron, F.; Páez-Hernández, D.; Notter, F.-P.; Pritchard, B.; Bolvin, H.; Autschbach, J. Magnetic properties and electronic structure of neptunyl(VI) complexes: Wavefunctions, orbitals, and crystal-field models. *Chem. Eur. J.* **2014**, *20*, 7994–8011.
- ⁷⁹ Gendron, F.; Pritchard, B.; Bolvin, H.; Autschbach, J. Single-Ion 4f Element Magnetism: an Ab-Initio Look at Ln(COT)₂⁻. *Dalton Trans.* **2015**, *44*, 19886–19900.
- ⁸⁰ Autschbach, J. Orbitals for Analyzing Bonding and Magnetism of Heavy-Metal Complexes. *Comments Inorg. Chem.* **2016**, *36*, 215–244.
- ⁸¹ La Mar, G. N.; Horrocks, W. D.; Holm, R. H. NMR of Paramagnetic Molecules. Academic Press: New York, 1973.
- ⁸² Köhler, F. H. Paramagnetic Complexes in Solution: The NMR Approach. In *eMagRes*, **2007**, John Wiley.
- ⁸³ Köhler, F. H. Probing Spin Densities by Use of NMR Spectroscopy. In *Magnetism: Molecules to Materials I*; Miller, J. S., Drillon, M., Eds.; Wiley-VCH Verlag GmbH & Co. KGaA: Weinheim, FRG, **2001**; pp 379–430.
- ⁸⁴ Kurland, R. J.; McGarvey, B. R. Isotropic NMR Shifts in Transition Metal Complexes: The Calculation of the Fermi Contact and Pseudocontact Terms. *J. Magn. Reson. (1969)* **1970**, *2*, 286–301.
- ⁸⁵ Bertini, I.; Luchinat, C.; Parigi, G. *Magnetic Susceptibility in Paramagnetic NMR. Proc. Nucl. Mag. Res. Spec.* **2002**, *40*, 249-273.
- ⁸⁶ Benda, L.; Mareš, J.; Ravera, E.; Parigi, G.; Luchinat, C.; Kaupp, M.; Vaara, J. Pseudo-Contact NMR Shifts over the Paramagnetic Metalloprotein CoMMP-12 from First Principle. *Angew. Chem. Int. Ed.* **2016**, *55*, 14713-14717.
- ⁸⁷ Moon, S.; Patchkovskii, S. First-principles calculations of paramagnetic NMR shifts. In *Calculation of NMR and EPR Parameters. Theory and Applications*; Kaupp, M.; Bühl, M.; Malkin, V. G., Eds.; Wiley-VCH: Weinheim, **2004** pages 325–338.
- ⁸⁸ Van den Heuvel, W.; Soncini, A. NMR Chemical Shift in an Electronic State with Arbitrary Degeneracy. *Phys. Rev. Lett.* **2012**, *109*, 073001.
- ⁸⁹ Soncini, A.; Van den Heuvel, W. Communication: Paramagnetic NMR Chemical Shift in a

Spin State Subject to Zero-Field Splitting. *J. Chem. Phys.* **2013**, *138*, 021103.

⁹⁰ Autschbach, J. NMR Calculations for Paramagnetic Molecules and Metal Complexes. In *Annual Reports in Computational Chemistry*, Vol. 11; Dixon, D. A., Ed.; Elsevier: Amsterdam, **2015** pages 3–36.

⁹¹ Fusaro, L.; Casella, G.; Bagno, A. Direct Detection of ¹⁷O in [Gd(DOTA)]⁻ by NMR Spectroscopy. *Chem. Eur. J.* **2015**, *21*, 1955-1960.

⁹² Komorovsky, S.; Repisky, M.; Ruud, K.; Malkina, O. L.; Malkin, V. G. Four-Component Relativistic Density Functional Theory Calculations of NMR Shielding Tensors for Paramagnetic Systems. *J. Phys. Chem. A* **2013**, *117*, 14209-14219.

⁹³ Hrobárik, P.; Reviakine, R.; Arbuznikov, A. V.; Malkina, O. L.; Malkin, V. G.; Köhler, F. H.; Kaupp, M. Density Functional Calculations of NMR Shielding Tensors for Paramagnetic Systems with Arbitrary Spin Multiplicity. *J. Chem. Phys.* **2007**, *126*, 024107-19.

⁹⁴ Borgogno, A.; Rastrelli, F.; Bagno, A. Characterization of Paramagnetic Reactive Intermediates: Predicting the NMR Spectra of Iron(IV)-Oxo Complexes by DFT. *Chem. Eur. J.* **2015**, *21*, 12960-12970.

⁹⁵ Martin, B.; Autschbach, J. Temperature Dependence of Contact and Dipolar NMR Chemical Shifts in Paramagnetic Molecules. *J. Chem. Phys.* **2015**, *142*, 054108.

⁹⁶ Martin, B.; Autschbach, J. Kohn-Sham Calculations of NMR Shifts for Paramagnetic 3d Metal Complexes: Protocols, Impact of the Delocalization error, and Analysis of the Curious Amide Proton Shifts of a High-Spin Iron(II) Macrocyclic Complex. *Phys. Chem. Chem. Phys.* **2016**, *18*, 21051–21068.

⁹⁷ Awais Rouf, S.; Mares, J.; Vaara, J. Relativistic Approximations to Paramagnetic NMR Chemical Shift and Shielding Anisotropy in Transition Metal Systems. *J. Chem. Theory Comput.* **2017**, *13*, 3731–3745.

⁹⁸ Vaara, J.; Awais Rouf, S.; Mares, J. Magnetic Couplings in the Chemical Shift of Paramagnetic NMR. *J. Chem. Theory Comput.* **2015**, *11*, 4840-4849.

⁹⁹ Novotný, J.; Sojka, M.; Komorovsky, S.; Necas, M.; Marek, R. Interpreting the Paramagnetic NMR Spectra of Potential Ru(III) Metallodrugs: Synergy between Experiment and Relativistic DFT Calculations. *J. Am. Chem. Soc.* **2016**, *138*, 8432-8445.

¹⁰⁰ Bora, P. L.; Novotný, J.; Ruud, K.; Komorovski, S.; Marek, R. Electronic-Spin Structure and Metal-Ligand Bonding in Open-Shell Systems from Relativistic EPR and NMR: A Case Study of Square-Planar Iridium Catalyst. *J. Chem. Theory Comput.* **2019**, *15*, 201-214.

-
- ¹⁰¹ Pennanen, T. O.; Vaara, J. Nuclear Magnetic Resonance Chemical Shift in an Arbitrary Electronic Spin State. *Phys. Rev. Lett.* **2008**, *100*, 133002.
- ¹⁰² Köhler, F. H.; Lescouëzec, R. Highly Resolved Spin-Density Distribution in the Prussian-Blue Precursors Cs₂K[Fe(CN)₆] and Cs₂K[Mn(CN)₆]. *Angew. Chem. Int. Ed.* **2004**, *43*, 2571–2573.
- ¹⁰³ Baumgärtel, N.; Flambard, A.; Köhler, F. H.; Lescouëzec, R. Paramagnetic Hexacyanometalates. The Diversity of Spin Distribution Studied by ¹³C and ¹⁵N MAS NMR Spectroscopy. *Inorg. Chem.* **2013**, *52*, 12634–12644.
- ¹⁰⁴ Davis, D. G.; Kurland, R. J. Carbon-13 NMR of Paramagnetic Iron-Group Cyanides. *J. Chem. Phys.* **1967**, *46*, 388.
- ¹⁰⁵ McGarvey, B. R.; Pearlman, J. N¹⁴ Nuclear Magnetic Resonance of Paramagnetic Complexes. *J. Magn. Reson.* **1969**, *1*, 178-184.
- ¹⁰⁶ Cano, J.; Ruiz, E.; Alvarez, S.; Verdaguer, M.; Spin-Density Distribution in Transition Metal Complexes: Some Thoughts and Hints. *Comments on Inorganic Chemistry* **1998**, *20*, 27-56.
- ¹⁰⁷ La Mar, G. N.; Satterlee, J. D.; de Ropp, J. S. Nuclear Magnetic Resonance of Hemoproteins. In *The porphyrin handbook*; Kadish, K. M., Smith, K. M., Guilard, R., Eds.; Academic Press: San Diego, Calif., **2000**; Vol. 5, pp 185–298.
- ¹⁰⁸ Myers, W. K.; Duesler, E. N.; Tierney, D. L. Integrated Paramagnetic Resonance of High-Spin Co(II) in Axial Symmetry: Chemical Separation of Dipolar and Contact Electron–Nuclear Couplings. *Inorg. Chem.* **2008**, *47*, 6701–6710.
- ¹⁰⁹ Duelund, L.; Toftlund, H. Electron Paramagnetic Resonance Characteristics of Some Non-Heme Low-Spin Iron(III) Complexes. *Spectrochimica Acta Part A: Molecular and Biomolecular Spectroscopy* **2000**, *56*, 331–340.
- ¹¹⁰ La Mar, G. N.; Horrocks, W. D.; Holm, R. H. *NMR of Paramagnetic Molecules: Principles and Applications.*; Elsevier Science: Burlington, **2013**.
- ¹¹¹ Frenking, G. Understanding the nature of the bonding in transition metal complexes: from Dewar's molecular orbital model to an energy partitioning analysis of the metal-ligand bond. *J. Organomet. Chem.* **2001**, *635*, 9-23.
- ¹¹² Loshen, C.; Frenking, G. Quantum Chemical Investigations and Bonding Analysis of Iron Complexes with Mixed Cyano and Carbonyl Ligands. *Inorg. Chem.* **2004**, *43*, 778-784.
- ¹¹³ Engel, N.; Bokarev, S. I.; Suljoti, E.; Garcia-Diez, R.; Lange, K. M.; Atak, K.; Golnak, R.; Kothe, A.; Dantz, M.; Kuhn, O.; Aziz, E. F. Chemical Bonding in Aqueous Ferrocyanido: Experimental and Theoretical X-ray Spectroscopic Study. *J. Phys. Chem. B* **2014**, *118*, 1555-

1563.

¹¹⁴ Autschbach, J.; Patchkovskii, S.; Pritchard, B. *J. Chem. Theory Comput.* **2011**, *7*, 2175–2188.

¹¹⁵ Hocking, R. K.; Wasinger, E. C.; de Groot, F. M. F.; Hodgson, K. O.; Hedman, B.; Solomon, E. I. Fe L-Edge XAS Studies of $K_4 [Fe(CN)_6]$ and $K_3[Fe(CN)_6]$: A Direct Probe of Back-Bonding. *J. Am. Chem. Soc.* **2006**, *128*, 10442-10451.

¹¹⁶ Schweizer, J. Polarized Neutrons and Polarized Analysis. In *Neutron Scattering from Magnetic Materials*; Chatterji, T., Ed.; Elsevier: **2006** pages 153–213.

¹¹⁷ Zhong, L.; Wen, X.; Rabinowitz, T. M.; Russell, B. S.; Karan, E. F.; Bren, K. L. Heme Axial Methionine Fluxionality in Hydrogenobacter Thermophilus Cytochrome C552. *Proc. Nat. Ac. Sci.* **2004**, *101*, 8637–8642.

¹¹⁸ Knorr, R.; Hauer, H.; Weiss, A.; Polzer, H.; Ruf, F.; Löw, P.; Dvortsák, P.; Böhrer, P. Unpaired Spin Densities from NMR Shifts and Magnetic Anisotropies of Pseudotetrahedral Cobalt(II) and Nickel(II) Vinamidine Bis(Chelates). *Inorg. Chem.* **2007**, *46*, 8379–8390.